ChemComm

ROYAL SOCIETY OF CHEMISTRY

FEATURE ARTICLE

View Article Online
View Journal | View Issue

Cite this: *Chem. Commun.*, 2025, **61**, 2636

Transition metal phosphide-based oxygen electrocatalysts for aqueous zinc–air batteries†

Santanu Ghora, Rishika Chakraborty, Saheb Bag, Mopidevi Manikanta Kumar and C. Retna Raj *

Electrically rechargeable zinc–air batteries (ZABs) are emerging as promising energy storage devices in the post-lithium era, leveraging the oxygen reduction reaction (ORR) and the oxygen evolution reaction (OER) at the air cathodes. Efficient bifunctional oxygen electrocatalysts, capable of catalyzing both the ORR and OER, are essential for the operation of rechargeable ZABs. Traditional Pt- and RuO_2/IrO_2-based catalysts are not ideal, as they lack sufficient bifunctional ORR and OER activity, exhibit limited long-term durability, require high overpotentials and are expensive. In contrast, non-precious metal-based catalysts, including transition metal phosphides (TMPs), have gained significant attention for their promising bifunctional catalytic properties, making them attractive candidates for ZABs. Despite encouraging lab-scale achievements, translating these advancements into market-ready applications remains challenging due to suboptimal energy performance. Rationally engineered bifunctional TMPs hold great potential for overcoming these challenges and meeting the requirements of rechargeable ZABs. This feature article reviews recent progress in the development of TMP-based catalysts for ZABs, providing a comprehensive overview of ZAB fundamentals and strategies for catalyst design, synthesis, and engineering. A particular emphasis is placed on widely studied bifunctional Fe, Co, and Ni phosphides, along with approaches to enhance their catalytic performance. Key performance metrics are critically evaluated, including the potential gap (ΔE) between the ORR and the OER, specific capacity, peak power density, and charge–discharge cycling stability. Finally, this feature article discusses the challenges faced in TMP-based ZABs, proposes strategies to address these issues, and explores future directions for improving their rechargeability to meet the demands of commercial-scale energy storage technologies.

Received 15th October 2024,
Accepted 20th December 2024

DOI: 10.1039/d4cc05498a

rsc.li/chemcomm

Functional Materials and Electrochemistry Lab, Department of Chemistry, Indian Institute of Technology Kharagpur, Kharagpur, 721302, West Bengal, India. E-mail: crraj@chem.iitkgp.ac.in

† Electronic supplementary information (ESI) available. See DOI: https://doi.org/10.1039/d4cc05498a

Santanu Ghora

Santanu Ghora received his BSc in Chemistry from Jadavpur University, West Bengal, in 2017 and completed his MSc in Chemistry at IIT Hyderabad, Telangana in 2019. In the same year, he joined the Department of Chemistry at IIT Kharagpur, West Bengal, India, to pursue his PhD under the supervision of Prof. C. Retna Raj. His research is dedicated to the synthesis and characterization of advanced electrocatalysts, including intermetallics, transition metal phosphides, and heterostructures, with a focus on their applications in high-performance zinc-air batteries and catalytic systems.

Rishika Chakraborty

Dr Rishika Chakraborty received her PhD degree in '1D and 2D Nanostructures: Design, Synthesis, Properties and Supercapacitor Application,' from National Institute of Technology (NIT) Meghalaya, India. She is currently a SERB-National Post Doctoral Fellow (N-PDF) at Department of Chemistry, Indian Institute of Technology (IIT) Kharagpur, India. Her current work is focused on the development of bifunctional oxygen electrocatalysts for zinc–air battery applications.

1. Introduction

The United Nations' World Population Prospects 2024 forecasts continued global population growth over the next 50 to 60 years, culminating in a projected peak within this century.[1] This demographic trend is driving an unprecedented increase in global energy demand. Concurrently, concerns regarding the depletion of non-renewable fossil fuel reserves and the associated greenhouse gas emissions are intensifying. Renewable energy sources, including solar, hydro, and wind, present viable alternatives for meeting the escalating industrial and domestic energy needs while fostering a sustainable ecosystem. However, the intermittency of these renewable sources poses significant challenges to power grid stability, necessitating effective balancing of electricity supply and demand. The transition to a low-carbon economy has catalyzed extensive research and development of energy conversion and storage systems. Electrochemical energy technologies, particularly rechargeable batteries and supercapacitors, have emerged as promising solutions for storing renewable energy and powering various applications, including electronic devices and electric vehicles (EVs). Lithium-ion batteries (LIBs), first commercialized by Sony Corporation in 1991, have revolutionized the market, establishing themselves as the primary energy source across diverse electronic platforms, including EVs, due to their advantageous balance of energy density, longevity, and efficiency.[2] Undoubtedly, LIBs offer a fine balance of energy density, longevity, and efficiency. The global energy market is projected to reach a size of USD 182.53 billion by 2030, with an expected compound annual growth rate of 18.1% from 2022 to 2030.[3] Nevertheless, issues related to economic viability, safety, recyclability, and the complexities of lithium-ion chemistry remain areas of active investigation and concern.[4]

The growing demand for clean energy is directing attention towards sustainable and environmentally friendly energy technologies. Aqueous rechargeable metal–air batteries (MABs) are particularly promising for meeting sustainability objectives and providing a reliable power supply. Their semi-open design facilitates a continuous intake of air from the atmosphere, contributing to both reduced weight and cost-effectiveness. MABs typically comprise a metal anode (such as lithium, magnesium, aluminum, iron, calcium, or zinc), a porous air cathode, and an electrolyte. Specifically, aqueous lithium–air batteries (LABs) require a lithium-ion conducting separator to mitigate the risk of violent reactions between the lithium anode and water. The operational mechanism of rechargeable MABs involves the stripping and plating of the metal anode, along with the oxygen reduction reaction (ORR) and oxygen evolution reaction (OER) occurring at the air cathode during the discharge and charge cycles, respectively. LABs exhibit a remarkable theoretical energy density of 3458 W h kg^{-1} and a cell voltage of 2.96 V.[5] However, the high cost and reactivity of lithium present significant challenges for the design and safe operation of LABs, undermining their longevity and market competitiveness.[6] Although non-aqueous electrolytes can support higher energy densities, they often compromise on cost and safety. In comparison, aluminum–air (Al–air) and magnesium–air (Mg–air) batteries demonstrate impressive theoretical energy densities of 2796 W h kg^{-1} and 2840 W h kg^{-1}, with operating voltages of 2.71 V and 3.09 V, respectively, which are comparable to those of LABs.[7] Nevertheless, their practical

Saheb Bag

Saheb Bag received both his BSc and MSc degrees in Chemistry in 2016 and 2018, respectively, from Vidyasagar University, West Bengal, India. He is currently pursuing his PhD in the Department of Chemistry, Indian Institute of Technology Kharagpur under the supervision of Prof. C. Retna Raj. His current research focuses on developing functional materials for aqueous zinc-based batteries and hybrid capacitors.

Mopidevi Manikanta Kumar

Dr Mopidevi Manikanta Kumar received his PhD degree in Electrochemistry from Indian Institute of Technology Kharagpur (IIT KGP), India in 2024 under the guidance of Prof. C. Retna Raj. He obtained his MSc in Chemistry from Andhra University, Visakhapatnam, India in 2014 and his BSc from the same university in 2012. His research interests include functional materials for electrochemical energy conversion and storage devices such as Zn–air batteries, water electrolyzers, etc.

C. Retna Raj

C. Retna Raj is a Professor in the Department of Chemistry, Indian Institute of Technology Kharagpur. Since 2002 he has been leading the Functional Materials and Electrochemistry Lab at IIT Kharagpur. His main research work focuses on the design and development of new multifunctional materials for electrocatalysis and electrochemical energy storage.

applications are largely restricted by anode corrosion induced by the hydrogen evolution reaction (HER) and issues related to non-rechargeability stemming from thermodynamic limitations. Conversely, zinc–air (Zn–air) and iron–air (Fe–air) batteries can be rechargeable when their air cathodes are bifunctionally active. Zinc–air batteries (ZABs) offer several advantages, including enhanced safety, high stability, a cell voltage of 1.65 V, a theoretical energy density of 1084 W h kg^{-1}, low cost (~$10 per kW h), and abundant availability of raw materials (Fig. 1).[8,9]

The first primary ZAB was developed in the 1870s using Pt-loaded porous carbon.[10] Subsequent efforts[11] aimed at creating practical devices continued until the 1930s, when Heise and Schumacher[12] successfully manufactured and commercialized the first alkaline ZAB, featuring a waterproof porous carbon air cathode and a 20% sodium hydroxide electrolyte. By the late 1950s, miniaturized primary ZABs were demonstrated for low-current consumer applications, including hearing aids, remote communications, and railway signalling devices. Over time, primary ZABs evolved into rechargeable variants, significantly expanding their application range.[13,14] However, the rise of LIBs in the late 1990s led to a decline in ZAB development. A turning point emerged in the 2000s as the limitations of LIBs became increasingly apparent, spurring renewed interest in ZAB technology. Current research, driven by advancements in nanotechnology and materials chemistry, is focused on enhancing the overall performance of ZABs. For a comprehensive overview of the history of ZABs and the various catalysts utilized in air cathodes, readers are encouraged to refer to the relevant literature.[15]

Despite substantial research on the development of rechargeable ZABs, the commercialization aspect has not significantly expanded since their initial market introduction in 2017 by NantEnergy (formerly fluidic energy). The company reported a limited energy density of approximately 35 W h kg^{-1}, with no further breakthroughs reported to date.[16] Notably, a groundbreaking development in zinc–air hybrid flow batteries has been shown to outperform LIBs. The battery storage costs approximately $250 per kW h for an 8-hour system, decreasing to $100 per kW h for a 32-hour system and $60 per kW h for 100 h.[17] In contrast, LIBs typically cost roughly $300 per kW h for durations exceeding eight hours. This advancement could potentially transform the utility-scale energy-storage market.

2. Fundamentals and performance evaluation of rechargeable ZABs

2.1 Working principle

A typical rechargeable ZAB is configured with an air-breathing cathode and a zinc anode, separated by a membrane, and

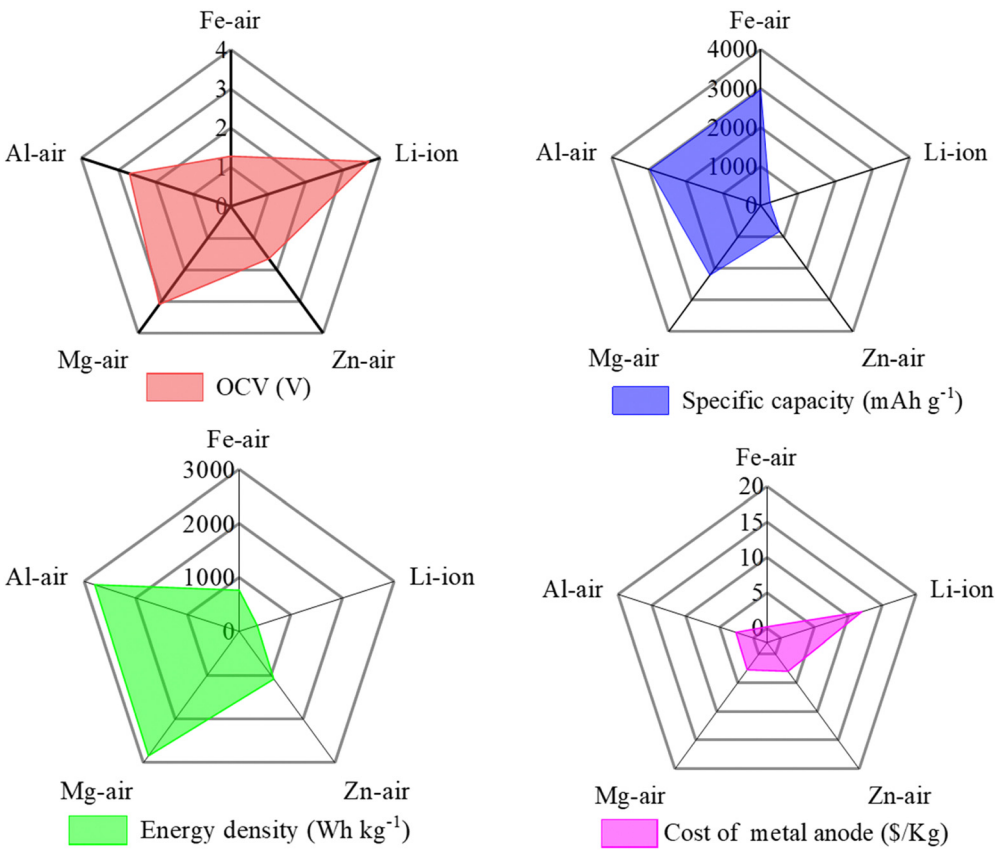

Fig. 1 Radar plot comparing the theoretical OCV, specific capacity, specific energy density, cost of metal anodes of Li-ion, Zn–air, Mg–air, Al–air, and Fe–air batteries.

utilizing an aqueous or gel electrolyte. The cathode and anode reactions of the ZAB are schematically represented in Fig. 2. During the discharge process, oxygen is reduced to hydroxide ions (OH^-) at the cathode, while the zinc anode undergoes oxidation, producing Zn^{2+} in the form of ZnO through the formation of a zincate ion. The deposition of ZnO over the Zn anode impairs the overall efficiency due to the insulating nature of ZnO. In contrast, the charging process involves the reverse reactions: the oxidation of hydroxide ions to oxygen at the cathode and the reduction of zinc ions back to metallic Zn at the anode, facilitating Zn plating.

The slow electron transfer kinetics associated with the ORR and OER at the air-cathode, as well as parasitic reactions and the HER at the anode, pose significant challenges in the advancement of efficient rechargeable ZABs. The HER not only corrodes the zinc anode but also reduces the overall lifespan of the battery. The direct four-electron reduction of oxygen to water is highly preferred, as the two-electron reduction generates hydrogen peroxide (HO_2^-), which can poison active sites and damage battery components due to its strong oxidizing properties. The air-cathode for a rechargeable ZAB requires an efficient bifunctional electrocatalyst that can facilitate the ORR and OER electron transfer kinetics at low overpotential. The ORR and OER involve complex reaction mechanisms with different active sites. The traditional Pt/C and Ir/Ru-based catalysts exhibit significant activity for the ORR and OER, respectively. However, these catalysts lack bifunctional oxygen electrocatalytic activity and demonstrate suboptimal long-term stability. Moreover, their less abundance largely limits their practical applications. In practical scenarios, the operating voltage of ZABs typically falls below 1.2 V, despite their standard cell voltage being 1.65 V (RHE). This voltage loss is primarily attributed to polarization effects in the ZABs, resulting in a notably low energy efficiency of $<60\%$.

2.2 Performance evaluation

The performance of a rechargeable ZAB should be evaluated in terms of specific capacity, energy density, power density, open circuit voltage (OCV), electrochemical stability, voltaic efficiency, and depth of discharge.

Specific capacity. The capacity refers to the total amount of charge in ZABs. The discharge capacity is the total amount of electricity generated during complete discharge at a given current density and time. It is estimated by considering the mass of zinc consumed after a full discharge and is expressed as

$$\text{Specific capacity} = \frac{\text{current} \times \text{time}}{\text{mass of Zn consumed}} \quad (1)$$

The theoretical specific capacity of ZABs is 820 mA h g_{Zn}^{-1}. However, several studies report the specific capacities exceeding the theoretical capacity without any rationale.[18,19] It is hypothesized that this discrepancy is possibly due to the lack of high-precision methods for measuring mass changes and the difficulty in cleaning the discharged anodes of the by-products that adhere firmly to the anode surface.

Energy density. It is the amount of energy stored in a given mass or volume; commonly normalized to the ratio of discharge capacity to the mass or volume of consumed zinc. It is generally obtained by multiplying the specific capacity with the operating voltage. The energy density of ZABs can be improved by increasing either the specific capacity or the operating voltage. With a high theoretical energy density of 1.084 kW h kg^{-1}, ZABs outperform currently available high-performance LIBs and are garnering significant interest for practical applications.[20] The energy density should be calculated by considering the total mass of the battery while comparing the performance of ZABs with other types of batteries, as the working voltage is largely different.

$$\text{Energy density} = \text{specific capacity} \times \text{discharge voltage} \quad (2)$$

Power density. Power density is the product of discharge current density and voltage, and commonly refers to the available energy output per unit mass or volume. It is generally observed that the power density decreases after a maximum while increasing the current density. The decline of power

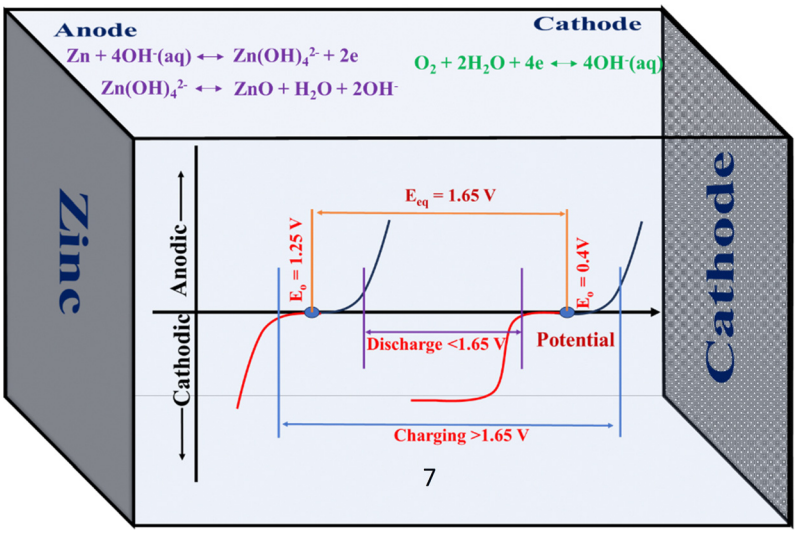

Fig. 2 Schematic illustration of the charge–discharge process of a rechargeable ZAB.

density at high current density is accounted for the Ohmic resistance and mass-transport limitation. The high electronic conductivity of the air cathode and facile charge transfer kinetics improve the power density. It is largely influenced by the cell configuration, air cathode design, type of separators and electrolytes, ORR activity and diffusivity of oxygen.[21]

$$\text{Power density} = \text{current density} \times \text{voltage} \quad (3)$$

Open circuit voltage (OCV). It is a basic thermodynamic property of a battery electrode and is the equilibrium voltage of a battery when no current flows.[22] It is an important parameter that provides the state-of-charge and state of health. The theoretical OCV of ZABs in an alkaline electrolyte is 1.65 V. However, the thermodynamic and kinetic limitations largely decrease the discharge voltage to 1.0 to 1.5 V.

Round-trip efficiency. The round-trip efficiency is the ratio of the total storage output to the storage input during one charge/discharge cycle and it can be described further in terms of voltaic efficiency and coulombic efficiency (also known as faradaic efficiency).

$$\text{(i) Voltaic efficiency} = \frac{\text{Average discharging voltage}}{\text{Average charging voltage}} \quad (4)$$

The discharge voltage of ZABs is generally lower than the charge voltage due to internal resistance and other factors.

$$\text{(ii) Columbic efficiency} = \frac{\text{Total charge extracted from the battery}\left(Q_{\text{discharge}}\right)}{\text{Total charge given into the battery}\left(Q_{\text{charge}}\right)} \quad (5)$$

The inverse of the coulombic efficiency is often called the charging factor.

Depth of discharge (DOD). It refers to the percentage of the capacity that is discharged during charge–discharge cycles relative to the overall capacity of the ZAB and is given by

$$\text{DOD} = \frac{\text{Capacity that is discharged during charge} - \text{discharge cycles}}{\text{Specific capacity of battery}} \quad (6)$$

3. Cathode electrocatalysts for ZABs

The performance of ZABs is primarily influenced by the air cathode, electrolyte, and anode. The design of an air cathode catalyst and the associated reaction mechanisms at the cathode are the most complex and critical factors determining overall battery performance. A significant challenge faced in ZABs is the sluggish electron transfer kinetics of the ORR and OER at the air cathode, which necessitates high overpotentials (η) and substantially reduces energy efficiency. The rational design, development, and optimization of durable bifunctional electrocatalysts are essential for enhancing electron-transfer kinetics at the triple-phase boundary. Such bifunctional catalysts not only improve electron transfer rates but also simplify cell design, reduce battery volume, and are of subsequently lower costs. Traditional electrocatalysts, such as Pt/C for the ORR and RuO_2/C or IrO_2/C for the OER, lack bifunctional activity and exhibit limited long-term durability under harsh electrolyte conditions. Furthermore, the loss of the electrochemically active surface area (ECSA) on extensive cycling, high cost, and scarcity significantly hamper their widespread application in large-scale settings.[23] In response, numerous non-precious catalysts are currently being synthesized and evaluated for the advancement of rechargeable ZAB technology.

In the pursuit of efficient non-precious electrocatalysts, transition metal-based materials, including oxides, sulfides, carbides, nitrides, and phosphides, have been extensively investigated for oxygen electrocatalysis. One of the major concerns in bifunctional oxygen electrocatalysis is that the ORR and OER processes have distinctive reaction pathways that require different active sites, necessitating careful selection of the catalyst. To facilitate efficient electron transfer kinetics for both the ORR and OER, the binding of oxygen species during bifunctional electrocatalysis must be optimized. Atomic-scale engineering of catalysts is a powerful approach to modulate the electronic structure, achieving optimal catalyst binding strength. The encapsulation of the active catalyst inside heteroatom-doped graphitic carbon, creating cation and anion vacancies, doping with metal cations, and heterostructuring have been explored to modulate the electronic properties.[24–33]

4. TMPs for oxygen electrocatalysis

The history of metal phosphides dates back to the 1700s with the synthesis of zinc phosphide, though it remained largely overlooked for many years.[34] Subsequently, several other metal phosphides including Ag_2P and Ni_2P were synthesized. Surprisingly, no further attempts have been made to understand their properties and application until the 1960s.[34] The metal phosphides are structurally complex and have distinctive physical, chemical, and electronic properties; the metal–phosphorus interaction and ratio (M/P) and the crystal structure control their properties.[35] The distinct properties arise from the high electronegativity of phosphorus (2.1), which induces electron delocalization between M and P, resulting in a partial charge on both metal and phosphorus ($M^{\delta+}$–$P^{\delta-}$) that mimic the hydrogenase enzyme.[36] Theoretical calculations indicate that the density-of-states (DOS) decreases from FeP to NiP and an increase in the P content further reduces DOS near the Fermi energy level.[37] The phosphorus atom also accounts for the durability of the electrocatalyst because the covalent M–P bond assures the stability of the catalyst.[36] Moreover, the atomic radius of the phosphorus (0.109 nm) allows TMPs to form triangular prismatic structures,[38] resulting in a higher number of unsaturated surface atoms and, consequently, enhanced catalytic activity.

It is essential to recognize that metallic M–M bonds coexist with both P–P and M–P bonds, providing the materials with enhanced chemical stability and mechanical strength. This coexistence also facilitates comprehensive compositional modifications of TMPs,

resulting in the formation of metal-rich phosphides (M_xP_y; $x > y$), stoichiometric phosphides (M_xP_y; $x = y$), and phosphorus-rich phosphides (M_xP_y; $y > x$).[39] Phosphorus-rich TMPs typically demonstrate greater activity toward the OER due to their abundant P–P bonding. Under high positive potentials, the phosphorus atoms oxidize into inorganic phosphate species and (oxy)hydroxides, which enhances surface wettability and significantly improves catalytic performance.[40] TMPs serve as pre-catalysts and the surface oxide/(oxy)hydroxide species generated on oxidation are the true active form of the electrocatalyst.[41] Metal-rich TMPs (MP or M_2P) with abundant metallic M–M bonding, exceptional chemical stability, and electronic conductivity exhibit great OER activity as was first observed in 1989 by Kupka and Budniok.[42]

4.1 Synthesis of TMPs

Earlier methods for synthesizing metal phosphides utilized harsh experimental conditions, employing flammable phosphorus or toxic phosphine as phosphidating agents. These approaches often resulted in uncontrolled particle size, morphologies, as well as phase impurities, which limited the large-scale production of phase-pure metal phosphides. Recent technological advancements have introduced new strategies for synthesizing nanoscale TMPs in various forms, including polycrystalline powders, thin films, nanoscale solids with diverse morphologies, and single crystals. The synthetic methods can be broadly classified into (i) solvothermal, (ii) solid-state, and (iii) electrochemical.

4.1.1 Solvothermal method. It involves the reaction of metal precursors (metal salts, organometallics, *etc.*) with the phosphidating reagents including tris(trimethylsilyl)phosphine ($P(SiMe_3)_3$), trioctylphosphine ($(C_8H_{17})_3P$, TOP), and triphenylphosphine ($(C_6H_5)_3P$, PP), at elevated temperatures (≥ 300 °C). TOP is preferred over the other phosphidating agents due to its cost-effectiveness. The low solubility and high decomposition temperature of these phosphidating reagents necessitate the use of high-boiling solvents such as 1-octadecylene, octyl ether, and squalene. Noble and non-noble metal phosphides were synthesized by injecting the corresponding metal precursor complex or preformed metal nanoparticles into TOP in high-boiling solvents at temperatures exceeding 300 °C. Schaak's group demonstrated a novel approach for the direct phosphidation of preformed metal nanoparticles with TOP in octlyether.[43] At elevated temperature, the C–P bonds in the TOP molecules are cleaved, allowing the phosphorus atoms to coordinate with the metal atoms and form TMP. High-quality nanostructured TMPs (FeP, MnP, Ni_2P, *etc.*) were synthesized through the thermal decomposition of the complexes and TOP.[44–47] Additional reagents or additives are required to achieve TMPs with the desired shape and size. Reports indicate that solvothermal reactions employing red and white phosphorus can produce TMPs at relatively low temperatures. For instance, hollow nanospheres of iron-doped nickel phosphide were synthesized *via* solvothermal phosphidation with white phosphorus in DMF at 180 °C.[48] Mono and multimetallic colloidal nanoparticle phases ($M_{2-x}M'_xP$; M, M′ = Fe, Co, Ni) have been obtained by reducing metal carbonyl or metal acetylacetonate precursors with oleylamine in the presence of a phosphidating agent and non-coordinating co-solvents.[49] The M : P ratio of TMPs can be adjusted by varying the amount of the phosphidating agent and reaction temperature.[50] The solvothermal synthesis of phase pure CoP required harsh reaction conditions in terms of the TOP quantity and reaction temperature compared to Co_2P.[51] While monodisperse phase-pure TMPs have been synthesized *via* a solvothermal method, the complex procedures involving high-boiling, flammable solvents, and air-free experimental setups significantly limit their scalability. A notable disadvantage of the solvothermal method is the requirement for oxygen-free synthetic environments, typically achieved using a glove box or Schlenk line.

4.1.2 Solid-state method. Solid-phase synthesis involves the homogeneous mixing of metal precursors and a phosphorus source in an ideal stoichiometric ratio, followed by high-temperature thermal treatment in a tube furnace under a reducing or inert atmosphere ($H_2/N_2/Ar$). The earliest report of synthesizing TMPs, specifically Ni_2P, using this solid-phase approach dates back to 1958.[52] This method was subsequently extended for the synthesis of bulk FeP in 1966.[53] In a traditional set up, the stoichiometric amounts of metal and red/black phosphorus were heated to a high temperature (>900 °C) for several days in an evacuated silica tube.[53] The complexities[54,55] like a long reaction time (1–10 days), and the formation of highly reactive and pyrophoric and toxic byproducts like P_4 and phosphine during high-temperature solid-state reactions led to the development of alternative methods employing other inorganic phosphidating agents such as PCl_3 (in molten $ZnCl_2$), $H_2PO_2^-$, HPO_3^{2-}, PH_3, and HPO_4^{2-} at elevated temperatures in an inert atmosphere.[56–59] Several TMPs like Cu_3P, Ni_2P, MoP, *etc.* have been obtained by thermal annealing of the physical mixture of the metal precursor and $H_2PO_2^-$ or $H_2PO_2^-$ impregnated metal precursors under inert gas flow.[56–59] One major advantage of using a phosphidating agent like hypophosphite is that the phosphidation can be achieved at a relatively low temperature of 200–300 °C. This method is known to produce smaller particles of uniform size as sintering of TMPs is largely avoided. The mechanism of phosphidation with hypophosphite involves the initial thermal decomposition of hypophosphite, producing PH_3, which subsequently reduces the metal precursor and phosphidates.[58] A modified approach resembling chemical vapor deposition has also been developed for the phosphidation of metal by onsite generated PH_3.[58] The corrosive and highly toxic nature of PH_3 is a matter of serious concerns. Conversely, the use of phosphate and phosphite for metal phosphidation requires a reducing atmosphere and elevated temperatures (500–700 °C).[59,60] The sintering of TMPs at such elevated temperatures cannot be avoided unless the reaction is performed over the catalyst support. Unlike the solvothermal synthetic approach, the desired shape and size of TMPs cannot be controlled in the solid-state synthetic methods.

To mitigate the problems associated with conventional solid-state strategies, our group has demonstrated universal solid-state strategies for the synthesis of heteroatom-doped carbon-encapsulated TMPs.[61–65] The nitrogen-doped carbon encapsulated MoP and WP core–shell nanostructures were

synthesized in two steps using phytic acid (PA) as a phosphidating agent.[61] This method involves the (i) self-assembling of polyoxometalate (M = Mo/W) and PA on the positively charged polyethylenimine (PEI) backbone, leading to the formation of supramolecular aggregates, and (ii) thermal decomposition of the aggregate in an inert atmosphere at 800 °C (Fig. 3). The metal precursors and PA are anionic due to the presence of abundant negatively charged oxygen atoms, while PEI is positively charged. The electrostatic and hydrogen bonding interactions of PA and the metal precursor with PEI are crucial for regulating the growth of metal phosphide. The key advantage of this method is the use of environmentally friendly PA as a phosphidating agent, while the supramolecular aggregate serves as the source of metals, P, N, and C. The mechanism involves the carbothermal reduction of the metal precursor and the subsequent phosphidation. Thermal annealing of the mixture of metal precursor and PA yields the corresponding pyrophosphate (MP_2O_7) underscoring the pivotal role of PEI. The self-assembled polyoxometalate is initially converted to pyrophosphate and then carbothermally reduced and phosphidated during the reaction. Furthermore, PEI facilitates the self-assembling of the metal precursors and PA, and serves as a carbon source for reducing the metal precursors. Subsequently, with the insights gained from the synthesis of MoP and WP core–shell nanostructures, we developed a novel approach for the general synthesis of TMPs using a single source precursor without additional phosphidating agents. The synthesis approach is very simple, and the product yield is very high. This approach involves the carbothermal reduction of a transition metal polypyridyl complex with the hexafluorophosphate counter anion to the corresponding TMP encapsulated with heteroatom-doped graphitic carbon.[62–64] In this method, the polypyridyl complex serves as a single-source precursor, with the counter anion serving as the phosphorous source. The growth of TMP largely depends on the amount of carbon. The growth of TMPs is highly dependent on the carbon content; an adequate amount of carbon, derived from either the coordinating ligands or external sources such as sucrose or melamine, is essential for the formation of phase-pure TMPs. In contrast, insufficient carbon results in the exclusive formation of pyrophosphate.[62] For instance, the thermal annealing of the tris(2,2′-bipyridine)cobalt(II) bis(hexafluorophosphate) ($[Co(bpy)_3](PF_6)_2$) or the bis(2,2′:6′2′-terpyridine)cobalt(II) bishexafluorophosphate ($[Co(terpy)_2](PF_6)_2$) complex produces only CoP_2O_7 while the bis(4′-pyridyl-2,2′:6′2′-terpyridine)cobalt(II)bis(hexaflurophosphate) ($[Co(pyterpy)_2](PF_6)_2$) complex yields the desired phase pure CoP. However, $[Co(terpy)_2](PF_6)_2$ as well as $[Co(bpy)_3](PF_6)_2$ complexes yield the desired CoP in the presence of a large excess of melamine or sucrose. Heteroatom-doped carbon-encapsulated phosphides of Co, Fe, and Ni were synthesized from the corresponding polypyridyl complexes using melamine/dicyanamide for electrochemical water splitting and bifunctional oxygen electrocatalysis (Fig. 4).[62–64] The thermal decomposition of the hexafluorophosphate anion produces $PF_5(g)$ in the temperature range of 200 to 600 °C[66] and the *in situ* generated $PF_5(g)$ is believed to phosphidate the metal. The annealing temperature significantly influences the crystallinity and electrocatalytic activity of the materials. The TMPs synthesized at 900 °C exhibit high crystallinity and enhanced activity compared to those obtained at lower temperatures.[63] In the synthesis of FeP, the encapsulating carbon was doped with nitrogen and phosphorus. The hexafluorophosphate anion acted as a phosphidating agent for metal and a doping agent of P.[63] The doping of phosphorus into carbon was not observed in the synthesis of other metal phosphides and the mechanism of P doping is not fully understood. The major advantage of this synthetic method is the high purity and crystallinity of TMPs, and the encapsulation of TMPs within graphitic carbon. The encapsulation enhances both the durability and catalytic activity of the TMPs. The synergistic interaction between the TMP core and the heteroatoms of the encapsulating carbon shell improves the catalytic performance. However, the TMP nanostructures obtained in this carbothermal reduction approach have a wide particle size distribution, ranging from 10 to 150 nm.

The size and shape of the nanoscale electrocatalysts play a decisive role in the catalytic activity primarily due to the change

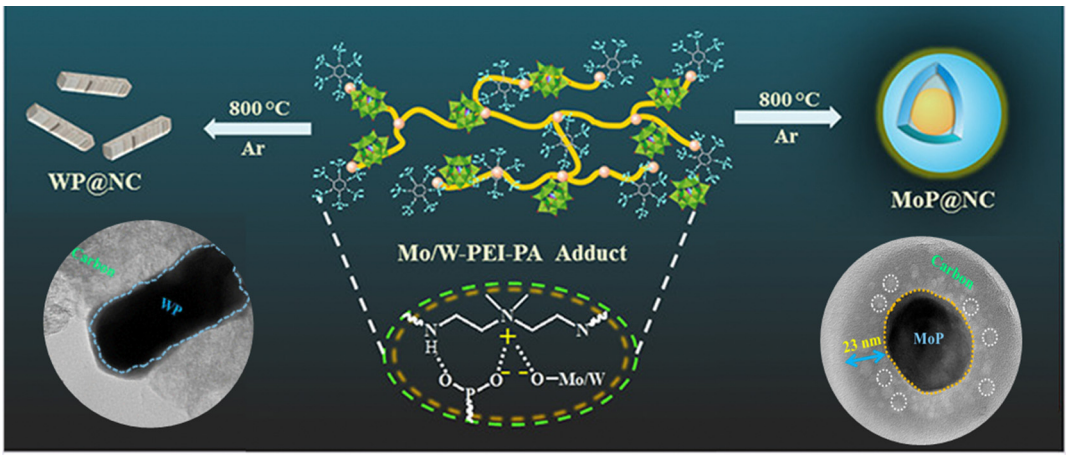

Fig. 3 Synthesis of MoP and WP core–shell nanostructures using phytic acid (PA) as a phosphidating agent. The TEM images of WP and MoP are given in the inset. Adapted from ref. 61.

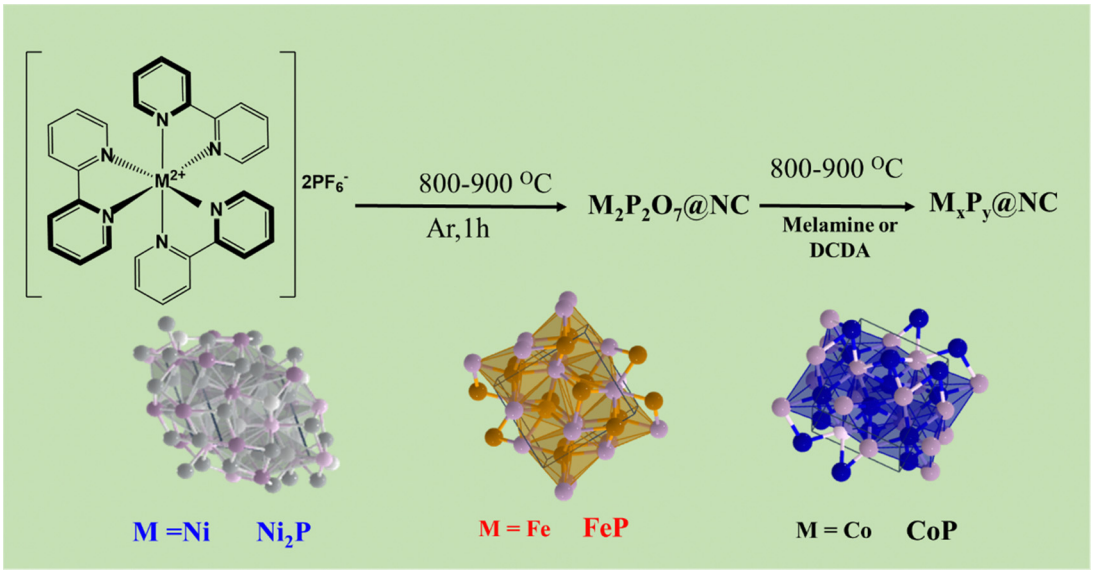

Fig. 4 Universal method for the synthesis of heteroatom-doped graphitic carbon encapsulated TMPs using a metal polypyridyl complex as a single source precursor. Ni_2P@NC, FeP@NC, and CoP@NC are synthesized using the corresponding polypyridyl complexes.

in the geometric and electronic properties. The effect of the particle size is closely linked to the catalyst's surface area, where variations in the size influence the coordination of surface atoms and, consequently, catalytic performance. It is well established that decreasing the particle size enhances catalytic activity; smaller particles not only provide a larger surface area but also exhibit modified intrinsic properties.[67] We successfully synthesized nitrogen and phosphorus-doped carbon-encapsulated OsP_2 (OsP_2@NPC) nanoparticles with an average size of 1.8 nm to achieve high electrocatalytic activity through a solid-state approach.[65] This involved the thermolysis of a homogeneous mixture of TPP, melamine, and ammonium hexachloroosmate(IV) at elevated temperature, resulting in near-monodispersed OsP_2@NPC. TPP serves both as a phosphidating and a doping agent (Fig. 5). Notably, thermal annealing of the osmium complex and melamine in the absence of TPP produced osmium nanoparticles encapsulated in nitrogen-doped carbon, underscoring the critical role of TPP in the phosphidation process. Interestingly, the nanosized OsP_2@NPC demonstrated exceptional electrocatalytic activity.

The P/M ratio, the reaction temperature and time, and the nature of the phosphidating agent significantly influence the growth and the properties of resulting TMPs. Nickel phosphides with different compositions, including M-rich phases (Ni_2P and Ni_5P_4) and P-rich phases (NiP_2 and NiP_3), were obtained by adjusting the P/M ratio.[68] The metal-rich phosphides are known for their metallic character,[69] while the P-rich

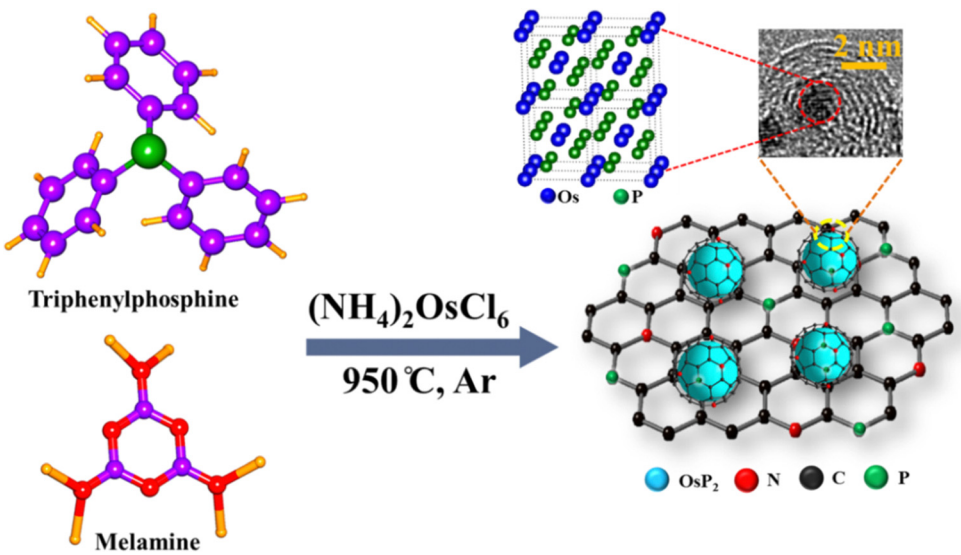

Fig. 5 Synthesis of OsP_2@NPC using TPP as a phosphidating agent. Reproduced with permission from ref. 65. Copyright 2019 Royal Society of Chemistry.

phosphides are highly stable in acidic media and exhibit promising catalytic activity.[70] In the impregnation-pyrolysis approach for the controlled synthesis of palladium phosphides (Pd_3P, Pd_5P_2, and PdP_2), the crystal phase of the phosphides is determined by fine-tuning the Pd/P ratio.[71] These Pd_mP_n catalysts exhibit varying catalytic performances despite having closely similar morphologies. Similarly, the degree of phosphidation of cobalt during the synthesis of Co_xP_y is controlled by adjusting the ratio of cobalt to phosphorus precursors.[72] The growth of monometallic phosphides and heterostructured phosphides from the same precursors has been achieved by tuning the reaction temperature. For instance, thermal annealing of the supramolecular gel precursor made of phosphidating agent PA, graphene oxide, Brij 58, and Co precursor $CoCl_2{\cdot}6H_2O$ at 900 °C in a reducing atmosphere yielded a CoP–Co_2P heterostructure. In contrast, annealing the same gel precursor at 800 °C and 1000 °C yielded CoP and Co_2P, respectively.[73]

4.1.3 Electrochemical method. The size-controlled chemical synthesis of electrocatalysts requires appropriate capping or stabilizing agents such as polymers and surfactants. While these agents are instrumental in controlling the particle size and shape, their presence can adversely affect electrocatalytic performance. Although the removal of capping agents through chemical or electrochemical treatments has been proposed, such processes often result in losing the nanoparticles' inherent catalytic activity. In the solid-state high-temperature synthesis methods, the uncontrolled growth of nanostructures due to sintering can detrimentally impact the catalytic activity. Furthermore, evaluating the electrocatalytic performance of nanoscale electrocatalysts typically involves modifying the electrode or current collector with the catalysts. This modification process requires a suitable binder and solvent to prepare a homogeneous catalyst ink; however, the presence of binders can also hinder the catalytic performance of nanoscale catalyst particles. In contrast, the direct growth (-supported) of well-defined nano- and microstructured TMPs on conductive substrates *via* an electrochemical or electroless approach offers several advantages. The electrodeposition method presents a promising alternative to the conventional synthetic approach to obtain self-supported catalysts with: (i) enhanced control over the amount of catalyst by optimizing the electrodeposition parameters, (ii) uniform dispersion of the catalyst without the need for capping or stabilizing agents, and (iii) selective growth of desired facet of the catalyst, and (iv) devoid of binders or solvents for dispersing the catalyst on the electrode surface. For the electrochemical deposition, 2- and 3-electrode electrochemical cells with current collectors such as metal foam, carbon cloth, and metal foils and neutral to acidic electrolytes have been used. Additives such as sodium citrate, Pluronic 123 (P123), 3-mercaptopropionic acid, *etc.*, are often used to control the surface morphology and structure (Table S1, ESI†). Ni and Cu foam current collectors afford highly porous nanostructures. The deposition is achieved with potentiostatic, galvanostatic, or pulse methods. In the potentiostatic methods, potential ranging from −0.3 to −1.2 V while current density ranging from 10 mA cm^{-2} to 2 A cm^{-2} are used. It should be pointed out here that the stoichiometric ratio of the metal precursors and deposition time largely decide the composition and crystal phase of the TMPs. It is recommended to use a metal/carbon foam current collector and the galvanostatic or pulse method for the deposition of TMPs.

The electrodeposition of phosphorus alloys with transition metals like Ni and Co dates back to the 1950s.[74] A Ni or Co alloy containing a maximum of 15% phosphorus was obtained in an acidic solution with phosphites and chloride or sulfate metal precursors at 75 °C, with current density ranging from 5 to 30 A dm^{-2}. The direct electrochemical growth of TMPs was further advanced between 1980s and 1990 with various bath compositions.[75] Early studies primarily focused on Ni and Co-based phosphides, with most electrochemical deposits resulting in amorphous materials. For instance, Ni- and Co-based phosphorus alloys (phosphides) were galvanostatically deposited at different current densities from a deposition bath containing NaH_2PO_2, sodium acetate, H_3BO_3, and NH_4Cl, along with the appropriate amount of metal precursor under normal temperature and pressure conditions.[76,77] The electrochemically grown amorphous Ni–Co–P and Co–P were thermally transformed into crystalline Co_2P and Ni_5P_2 at 773 K. Since then, various mono- and bimetallic phosphides have been electrochemically synthesized for different applications.[78,79] Additives such as glycine, oxalic acid, sodium citrate, boric acid, *etc.* have been utilized to control the electrodeposition. Various conducting substrates like carbon paper, carbon fibres, Pt, and nickel have been employed for deposition.

A reductive electrosynthetic approach is demonstrated recently for the synthesis of trimetallic Ni–Co–Mn phosphide using a structure-regulating agent P123 in an acidic electrolyte.[36] The morphology and composition of the trimetallic TMP are tailored by controlling the current density, deposition time, and bath composition. P123 played a crucial role in regulating the growth of porous Ni–Co–Mn–P. It non-covalently interacts with the metal precursors and adsorbs on a particular crystal facet. Such adsorption largely reduces the surface energy and favors the growth of selected facets. The pulse electrodeposition with the dynamic hydrogen bubble template approach has been demonstrated to produce hierarchically porous TMPs like NiCu–P, Ni–Fe–P, Cu–Co–P_x, *etc.* (Fig. 6).[80–82] The hydrogen bubbles generated on the electrode surface during the electroreduction of metal ions serve as a template for the convenient generation of a highly porous 3D dendritic structure. The phosphidating agent $H_2PO_2^-$ is also reduced to P during the reduction of metal ions on the electrode surface and diffuses to the metallic crystal lattice and yields TMPs. The pulse electrodeposition approach often yields hydrophilic/superhydrophilic TMPs as evidenced by small contact angles[80,83] and electrocatalytically high activity. The hydrogen bubble template significantly increases the electrochemically active surface area of the catalyst and the surface morphology and surface structure can be conveniently tailored by tuning the bath composition and pH, and electrochemical deposition parameters. The current collector (substrate) plays a significant role in regulating the surface morphology and porosity of TMPS. Carbon cloth and metal (Ni and Cu) foams/foils have been widely used and the metal foam substrates afford highly porous TMPs.

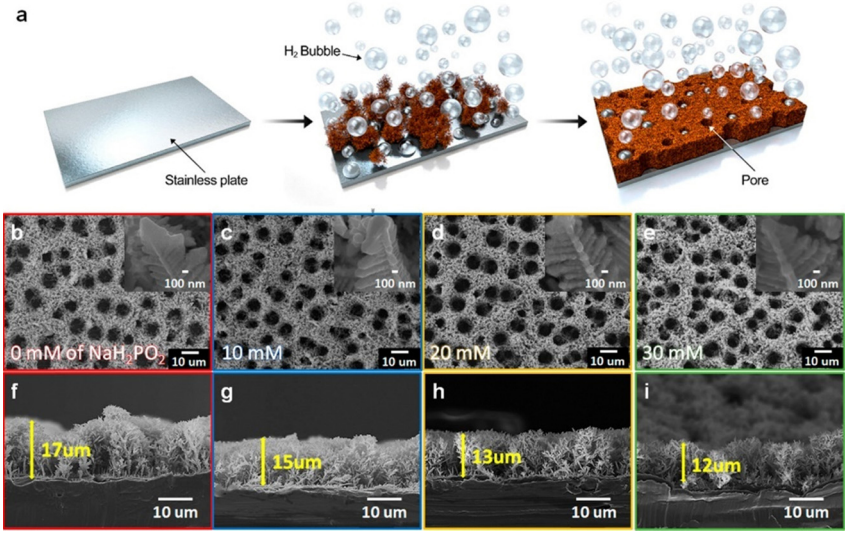

Fig. 6 (a) Schematic representation of pulse electrodeposition of TMPs using the dynamic hydrogen bubble template approach. (b)–(i) Corresponding FESEM image of synthesized porous TMPs. Reproduced with permission from ref. 82. Copyright 2019 American Chemical Society.

Two primary mechanisms for the electrodeposition of TMPs have been proposed: (i) direct and (ii) indirect mechanisms. In the direct mechanism, the precursor phosphorus oxyacid is partially reduced to hypophosphite in the negative potential region. The electrochemically generated hypophosphite is further reduced to P (eqn (7) and (8)).[84,85] It is important to note that the metalloids cannot be deposited alone; however, they can be co-deposited with the metals (induced co-deposition).[84] The metal cations and the hydrogen ions are reduced at negative potential to metal and hydrogen. The direct reduction of hypophosphite and metal ions is expected to produce an M–P alloy with a high P content (eqn (9) and (10)). In contrast, the indirect mechanism involves the *in situ* generation of PH_3 and the subsequent deposition of the M–P alloy (eqn (11) and (12)). The efficiency of the indirect mechanism is reported to be low as the generation of PH_3 from phosphorus oxyacid depends on the H^+ reduction. For a more comprehensive understanding of the electrodeposition mechanisms, readers are encouraged to consult the relevant literature.[84,86,87]

$$H_2PO_3 + 2H^+ + 2e \rightarrow H_2PO_2^- + H_2O \quad (7)$$

$$H_2PO_2^- + H^+ + e \rightarrow P + 2H_2O \quad (8)$$

$$M^{2+} + 2e \rightarrow M^0 \quad (9)$$

$$nM^0 + P \rightarrow M\text{–}P \quad (10)$$

$$H_2PO_3 + 6H^+ + 6e \rightarrow PH_3 + 3H_2O \quad (11)$$

$$2PH_3 + 3M^{2+} \rightarrow 2P + 3M + 6H^+ \quad (12)$$

5. Bifunctional oxygen electrocatalytic activity and ZAB performance of TMPs

A bifunctional catalyst designed for a rechargeable ZAB must have a large electrochemically active surface area, promote efficient electron transfer kinetics for both the ORR and OER and maintain long-term durability across a wide potential window under harsh electrolyte conditions. The synthetic approach significantly influences the catalyst's shape, surface morphology, and consequently, its surface area. A key challenge is minimizing the loss of the ECSA during prolonged cycling, which can result from agglomeration or dissolution of the catalyst. Naked catalysts often suffer from the loss of the ECSA while encapsulating the active catalyst with a thin layer of carbon or heteroatom-doped carbon enhances both durability and overall catalytic performance. This thin outer shell effectively prevents undesired dissolution without compromising the catalytic activity of the core material. However, the thick carbon shell can negatively impact the electron transfer kinetics. Most TMP-based catalysts are typically supported on carbon materials doped with heteroatoms, which are known to promote the ORR in alkaline environments. The oxygen electrocatalytic activity of carbon-encapsulated phosphides of first-row transition metals has been assessed for the development of rechargeable ZABs. The TMPs based on Fe, Co, and Ni demonstrate promising bifunctional activity for the charge and discharge reactions of ZABs (Tables S2–S4, ESI†). However, the high adsorption energy of hydrogen and oxygen intermediates on TMPs and the availability of a limited number of active sites largely limit the scaling up for practical applications.[88,89] In this article, TMP-based electrocatalysts are classified into three categories: monometallic, multimetallic, and heterostructured TMPs, with a discussion on their bifunctional performance.

5.1 Monometallic TMPs

Cheng *et al.* were the first to demonstrate the ORR activity of carbon-supported PdP synthesized *via* the hypophosphite route.[90] Subsequently, the electrocatalytic performance of precious and non-precious metal-based phosphides towards the ORR and OER has been investigated.[91–94] Among the TMPs, the cobalt- and iron-based phosphides received considerable

attention for the OER and ORR since 2015.[95–97] Despite the extensive studies on the OER activity of these phosphides for electrochemical water splitting, their bifunctional activity towards the ORR and OER was initially not well explored. For the first time, Zhong *et al.* demonstrated the bifunctional oxygen electrocatalytic activity of an integrated catalyst consisting Co_2P and Co_xN encapsulated in an amorphous nitrogen-doped carbon shell.[98] Although this integrated catalyst did not achieve a theoretical current density of ~6 mA cm^{-2} for the ORR, it exhibited a reasonable OER activity, resulting in an overall oxygen electrode activity ($\Delta E = E_{OER} - E_{ORR}$) of 0.84 V. The rechargeable ZAB delivered a maximum power density of only 87.3 mW cm^{-2} with an OCV of 1.43 V. Subsequently, Manthiram's group investigated the bifunctional activity of CoP integrated with heteroatom doped graphitic carbon, achieving an ΔE of 0.74 V and demonstrating charge–discharge cycling stability for the ZAB for over 450 h without significant voltage loss (Fig. 7).[99] The heteroatom-doped carbon plays a significant role in enhancing the ORR activity, while the *in situ* generation of cobalt oxide—resulting from the oxidation of cobalt phosphide at high positive potentials—contributes to the OER activity. In recent years, several cobalt- and iron-based phosphides encapsulated or supported on appropriate carbon materials have been synthesized for use in ZABs.[100–104] The CoP/Co_2P-based catalysts exhibited a ΔE ranging from 0.65 to 0.93 V, peak power densities between 65 and 226 mW cm^{-2}, and charge–discharge cycling stability lasting from 23 to 407 hours at a current density of 10 mA cm^{-2}. On the other hand, Fe-based phosphides demonstrated impressive oxygen electrocatalytic performance, achieving a discharge capacity of 654–805 mA h cm^{-2} at 10 mA cm^{-2} and power densities of 80–190 mW cm^{-2} (Table S2, ESI†).

Our group developed a novel approach for synthesizing heteroatom-doped graphitic carbon encapsulated monometallic TMPs (CoP, FeP, and Ni_2P) using a single-source precursor (*vide supra*) and investigated their bifunctional oxygen electrocatalytic activity. The heteroatom-doped carbon-encapsulated CoP (NC-CoP), derived directly from $[Co(pyterpy)_2](PF_6)_2$ without additional carbon and nitrogen sources, exhibited ΔE of only 0.84 V though it could promote the 4-electron reduction of oxygen to water, with an onset potential and a limiting current density of 0.82 V and 5.2 mA cm^{-2} (1600 rpm).[62] It has limited ZAB performance, suffering over 2.5% voltaic efficiency loss after 30 h of charge–discharge cycling (Fig. 8). The limited bifunctional activity of NC-CoP can be attributed to the insufficient amount of heteroatom-doped carbon, which is necessary for synergistically enhancing the oxygen electrocatalysis and protecting the active CoP catalyst from aggregation and surface passivation. Moreover, the NC-CoP catalyst has the Brunauer–Emmett–Teller (BET) specific surface area of only 120 m^2 g^{-1} with a small average pore size of 3.8 nm. On the other hand, the CoP catalyst (CoP@NC) synthesized from $[Co(bpy)_3](PF_6)_2$ in the presence of an additional carbon and nitrogen source (melamine) demonstrated improved bifunctional oxygen electrocatalytic activity with a ΔE of 0.75 V. The BET surface area (190 m^2 g^{-1}) and the average pore size (21 nm) of CoP@NC are significantly higher than those of NC-CoP (*vide supra*). Unlike the NC-CoP catalyst, CoP particles in CoP@NC are encapsulated with nitrogen, resulting in a synergistic interaction between the core CoP and the encapsulating nitrogen-doped carbon (NC). This synergistic effect improves the electron transfer kinetics for the ORR.[62–64] The observed decrease in ΔE (~ 100 mV) compared to NC-CoP underscores the critical importance of the surface area and the encapsulation of the active catalyst with heteroatom-doped carbon. The rational heterostructure engineering of CoP@NC further improves the oxygen bifunctional activity (*vide infra*).

The FeP nanoparticles encapsulated within a N, P dual-doped graphitic carbon matrix (FeP@NPC) synthesized *via* carbothermal reduction-assisted phosphidation showed excellent catalytic activity for both the ORR and OER. The ORR onset potential was measured to be 0.975 V, which is comparable to that of the state-of-the-art Pt/C catalyst while displaying a small ΔE of 670 mV in 0.1 M KOH (Fig. 9). The ZAB exhibited a peak power density of 190.15 mW cm^{-2}, an energy density of 706.5 W h kg_{Zn}^{-1}, and a specific capacity of 785 mA h g_{Zn}^{-1} at 50 mA cm^{-2}.[63] Remarkably, the ZAB retained its initial voltaic efficiency, exhibiting only 0.9% loss after extended charge–

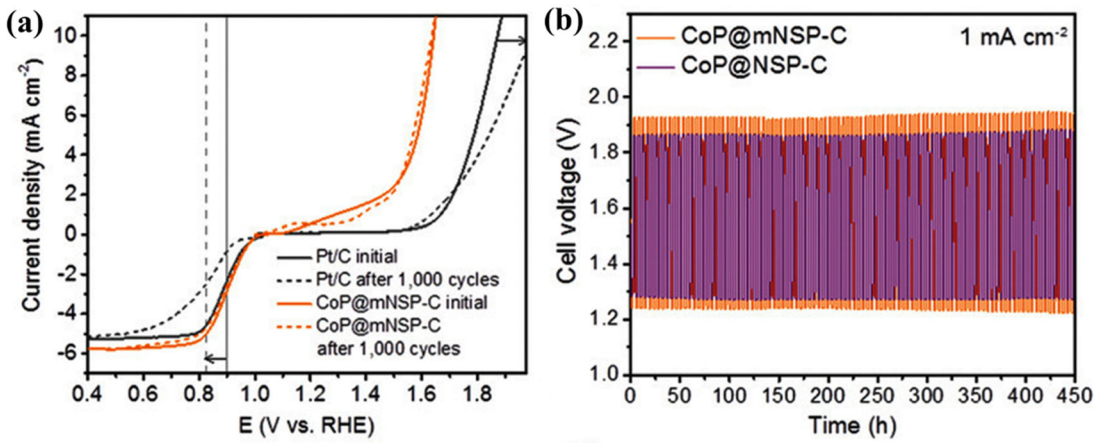

Fig. 7 (a) Polarization curves illustrating the bifunctional electrocatalytic activity of CoP integrated with heteroatom-doped carbon. (b) Charge–discharge cycling performance at 1 mA cm^{-2} of the rechargeable ZAB. Reproduced with permission from ref. 99. Copyright 2017 Wiley.

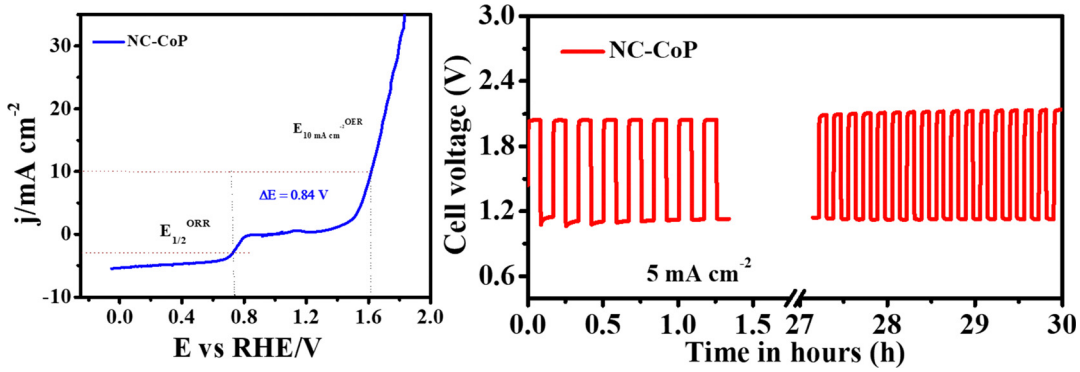

Fig. 8 (a) Polarization curves illustrating the bifunctional electrocatalytic activity of NC-CoP. (b) Charge–discharge cycling performance at 5 mA cm^{-2} of the rechargeable ZAB.

discharge cycles. The bifunctional activity of FeP@NPC is significantly higher than that of the other FeP catalysts obtained from iron phytate precursors. The enhanced activity is attributed to the synergistic interaction between the FeP core and the encapsulating defect-rich carbon network, increased oxygen affinity, and modulation of the electronic properties of the carbon network due to phosphorus doping, as well as the substantial presence of pyridinic nitrogen (approximately 57%), which interacts favorably with FeP. Oxygen-containing species, including FeOOH/Fe–OH generated on the surface during the anodic sweep, efficiently catalyze the OER. FeP@NPC is highly active towards electrochemical water splitting and the ZAB could power an alkaline water-splitting cell for over 24 h without any significant attenuation of OCV. The ideal integration of the heteroatom-doped graphitic carbon with the FeP core boosts the bifunctional activity and durability. A wood-derived monolithic FeP catalyst showed good oxygen electrocatalytic activity with a ΔE of 680 mV.[102] The DFT studies indicated that FeP facilitates the activation of water molecules, promoting the efficient dissociation of water to generate H^+ ions necessary for the ORR. The ZAB delivered a specific capacity of 805 mA h g_{Zn}^{-1} at 10 mA cm^{-2}, although the peak power density is limited to 144 mW cm^{-2}. Furthermore, the solid-state ZAB delivered a peak power density of 59 mW cm^{-2} and maintained long charge–discharge cycling stability for over 40 h.

Nickel phosphide-based catalysts demonstrate significant potential for electrochemical water splitting due to their efficient formation of the oxygen intermediate *OOH.[106,107] However, investigations into the ORR activity of nickel phosphides remain limited, likely due to the inferior activity of the pristine nickel phosphides.[108,109] The MOF-derived Ni_xP-NPC hybrid catalyst exhibits good bifunctional oxygen activity, characterized by an ORR onset potential of ~0.9 V and an average H_2O_2 yield of 20%.[110] Notably, the catalyst fails to produce a well-defined ORR polarization curve, indicating sluggish electron transfer kinetics. Despite these limitations, the ZAB utilizing this catalyst achieves a power density of 266 mW cm^{-2} and demonstrates charge–discharge stability for ~30 hours. It is surprising to observe such high-power density when the ORR kinetics is sluggish with an average H_2O_2 yield of 20%.

5.2 Strategies to improve the electrocatalytic activity

The crystal structure and composition of TMPs have a distinct role in the bifunctional oxygen electrocatalytic activity. Despite the advantages of the unique electronic structure, the electrocatalytic performance of pristine monometallic TMPs is limited

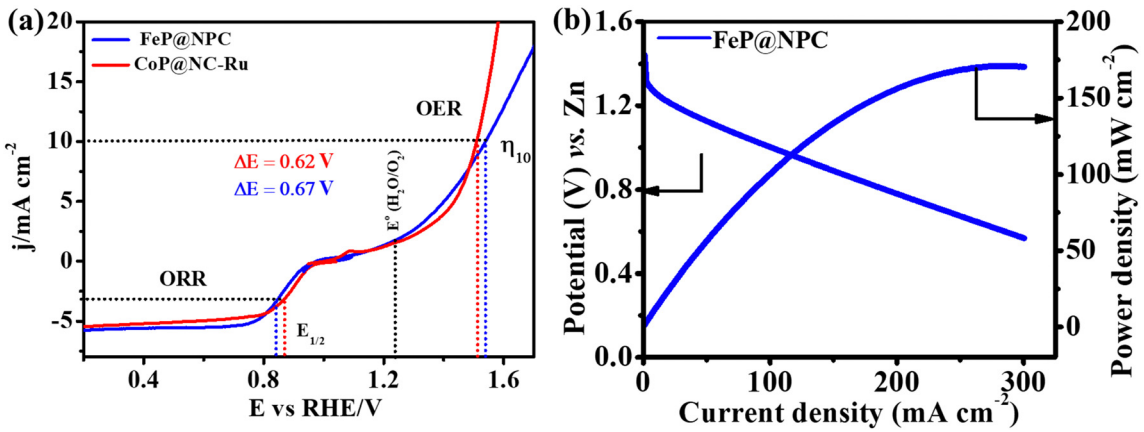

Fig. 9 (a) Polarization curves of FeP@NPC and CoP@NC-Ru demonstrating their bifunctional oxygen activity. (b) Discharge polarisation curve of FeP@NPC showing the power density. Adapted from ref. 63 and 105.

compared with that of the noble metal-based catalysts. Several engineering strategies are adopted to boost the oxygen electrocatalytic activity and ZAB performance (Tables S3 and S4, ESI†). The engineering strategies are classified into (i) P anion and metal cation vacancy defect engineering, (ii) doping engineering and synthesis of bimetallic/trimetallic phosphides, and (iii) heterostructure engineering. The engineered TMPs have significantly improved catalytic performance in terms of ΔE, discharge capacity, power density, and charge–discharge cycling stability.

5.2.1 Vacancy engineering. Defect engineering, where vacancies are introduced into the TMP lattice, is a promising strategy to boost the electrocatalytic activity. It modulates the electronic structure and influences the binding strength of the reactant and reaction intermediates. Vacancy defects modify the local atomic structure and the coordination number of TMPs, exposing abundant catalytically active sites.[111] The anion-vacancy defects can enhance the electronic conductivity of catalysts and optimize the adsorption energies of intermediates involved in the electrocatalytic reactions.[112] Specifically, the P-vacancies in TMPs enhance the OER activity by reconstructing the electronic states and generating new active sites.[113] They shift the d-band center closer to the Fermi level, thereby improving the electrocatalytic activity.[114] The P-vacancies can induce the formation of O-vacancies during the positive potential sweep, promote the facile formation of metal oxyhydroxide, and enhance the OER performance.[115,116] The existing methods for creating vacancies primarily involve expensive plasma etching or reduction with $NaBH_4$. Integrating P-vacancy-rich nickel phosphide with heteroatom-doped carbon presents an ideal approach for boosting the electrocatalytic performance of nickel phosphide.[64] Recent studies have demonstrated that vacancy engineering can modulate the bifunctional oxygen electrocatalytic activity of nitrogen and phosphorus dual-doped carbon encapsulated Ni_2P (Ni_2P@NPC). The Ni_2P@NPC catalyst was synthesized from single-source precursors (Fig. 4) and subsequently engineered through acid treatment. This treatment exfoliates the encapsulating heteroatom-doped graphitic carbon and increases the number of P vacancies as well as the surface area of the catalyst. The removal of carbon debris and the generation of P vacancies enhance the number of active sites by exposing redox centres to the electrolyte, with surface coverage increasing from 0.26×10^{-8} to 0.47×10^{-8} mol cm^{-2} (Fig. 10). The P-vacancy-rich Ni_2P@NPC showed a good ORR and OER activity with an ORR onset potential of 0.9 V. The exchange current densities for the ORR (2.62×10^{-7} mA cm^{-2}) and the OER (0.4×10^{-5} A cm^{-2}) for the engineered catalyst are higher than those of the as-synthesized catalyst, underscoring the importance of P-vacancy engineering in oxygen electrocatalysis. The ZAB made using the vacancy-engineered Ni_2P@NPC delivers a power density of 162 mW cm^{-2}, a specific capacity of 770.25 mA h g^{-1}, and an energy density of 692 W h kg^{-1}. The device demonstrates long cycling stability for over 100 hours, with only a 0.6% loss in voltaic efficiency (Fig. 11). The enhanced activity is attributed to the high nitrogen content, the substantial number of electrochemically active sites, and the facile formation of active surface oxyhydroxide/hydroxide species during the OER. Nickel phosphonate-derived P-vacancy-rich Ni_2P

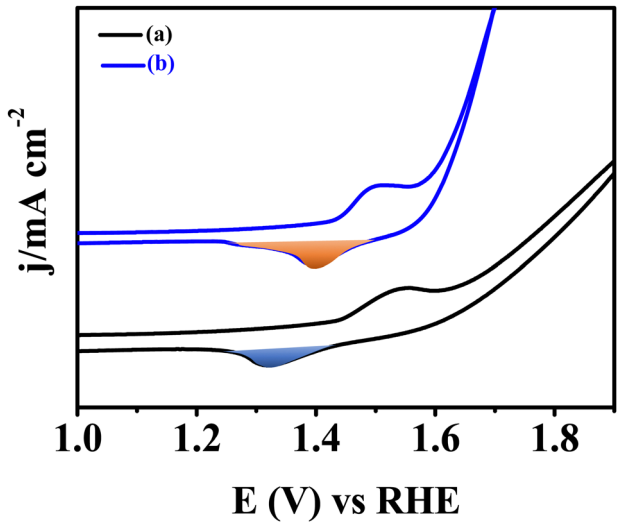

Fig. 10 Cyclic voltammogram illustrating the effect of surface-engineering on the surface covered with nickel. (a) As-synthesized and (b) surface-engineered Ni_2P@NPC. Adapted from ref. 64.

obtained through carbonization followed by argon plasma treatment also exhibits decent oxygen electrocatalytic activity, with a ΔE of 0.70 V and a power density of 203 mW cm^{-2}.[110] The synergistic interaction between heteroatom-doped carbon and the P-vacancy-rich Ni_2P is accounted for the enhanced activity. The catalyst could deliver a ORR limit current density of only ~4.2 mA cm^{-2} though it has good onset potential.

The cation vacancy defects also modulate the electronic properties of TMPs and improve their catalytic performance. Cation vacancy-rich TMPs are very promising for electrochemical water splitting.[117] However, the bifunctional oxygen electrocatalytic performance of cation vacancy-rich TMPs is not explored. The cation vacancy defects in TMPs can enhance the ORR reaction kinetics and deliver high discharge specific capacity.

5.2.2 Doping engineering and bimetallic phosphides. The introduction of one or more metals to create multi-metallic phosphides typically enhances catalytic performance compared to their corresponding monometallic phosphides. In this article, TMPs with a small amount of a second metal are referred to as metal-doped TMPs. Conversely, when a sufficiently high concentration of both metals is employed, the resulting TMPs are classified as bimetallic phosphides, which exhibit distinct properties due to the formation of an independent bimetallic phase. It is well established that bimetallic phosphides demonstrate superior electrocatalytic performance relative to their monometallic counterpart. Incorporating a secondary metal into phosphides enables synergistic modifications in the composition and electronic structure of the surrounding core metal, leading to an enhanced electrochemical performance. However, synthesizing bimetallic phosphides presents challenges, as conventional methods often yield heterostructures comprising two distinct monometallic phosphides.[118,119] The electrocatalytic activity of these heterostructured TMPs will be discussed in the following section. To achieve the desired bimetallic phosphides, it is crucial to optimize synthetic procedures and carefully select metal precursors.

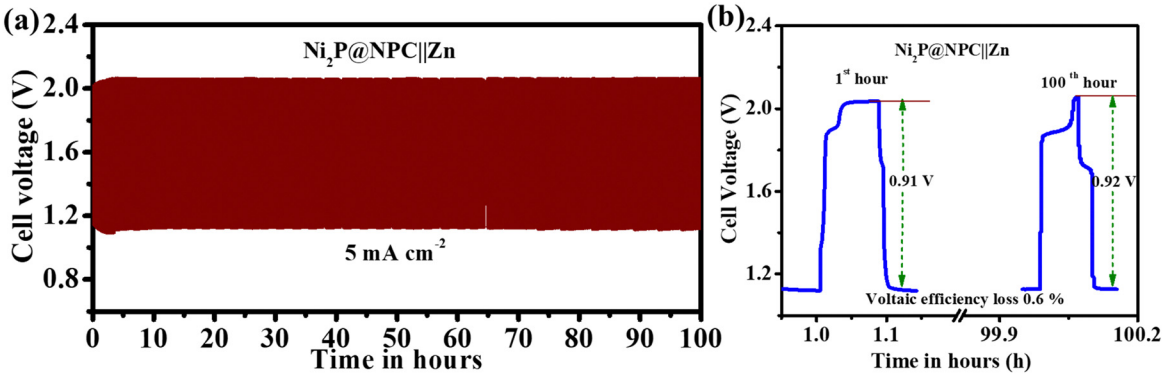

Fig. 11 (a) Galvanostatic charge–discharge cyclability of the Ni_2P@NPC-based ZAB at 5 mA cm^{-2}. (b) Voltaic efficiency plots of Ni_2P@NPC||Zn. Reproduced with permission from ref. 64. Copyright 2024 Wiley.

Doping of a second metal into TMPs has a profound influence on the electrocatalytic activity toward water splitting[120] as in the case of vacancy engineering. It alters their intrinsic properties and boosts the electrocatalytic performance. The metal-doping effect on the bifunctional oxygen electrocatalysis has recently been explored. The metal-doped (Mn, Cu, Cr, Co, *etc.*) TMPs deliver power density in the range of 40 to 224 mW cm^{-2} and OCV ranging from 1.35 to 1.5 V.[121–124] The doping of Cu into Co_2P weakens the binding of adsorbed oxygen intermediates and accelerates the ORR electron transfer kinetics.[125] A specific capacity of 736 mA h g_{Zn}^{-1} and a power density of 236 mW cm^{-2} were achieved with the ZAB. The doping of Co into the FeP lattice modifies the d-band center of Fe and accelerates the proton-coupled electron transfer reaction for the 4-electron reduction of oxygen to water.[126] The theoretical studies showed that the d-band center of Co-doped FeP is closer to the Fermi level compared to the undoped FeP. The Co-doped FeP has excellent oxygen electrocatalytic activity with a ΔE of 650 mV and a power density of 152 mW cm^{-2} is achieved with the ZAB. The device has extended charge–discharge cycling stability for 800 hours at 10 mA cm^{-2} without significant change in the voltage gap. The quasi-solid ZAB delivers a power density of 72 mW cm^{-2} and an OCV of 1.44 V and it has good charge–discharge cyclability for >150 cycles (Fig. 12). The W-doped Co_2P catalyst has effectively facilitated the four-electron reduction of oxygen, exhibiting a half-wave potential of 0.86 V and a ΔE of 0.72 V.[124] Notably, the specific capacity due to utilizing this catalyst is reported to be 881 mA h g^{-1}, exceeding the theoretical specific capacity of zinc, which is 820 mA h g^{-1}. Additionally, Fe-doped CoP has been evaluated for use in Li–O_2 batteries and exhibited a high discharge-specific capacity.[127] The incorporation of a sufficient amount of second metal into the lattice of parent TMPs leads to the formation of bimetallic phosphides. This integration modifies the electronic properties and enhances electron transfer kinetics at the bimetallic interface. By employing surface engineering and electronic modification strategies, the electrocatalytic properties of monometallic TMPs have been optimized. The addition of oxophilic metals, such as Co, is anticipated to further regulate the electronic properties and improve catalytic activity.

The bimetallic TPMs based on Ni, Co, and Fe have shown promising oxygen bifunctional activity with ΔE values of 0.66 V to 0.86 V and specific capacity in the range of 602–793 mA h g^{-1} at 10 mA cm^{-2}, and a power density of 122–183 mW cm^{-2} is achieved[128–131] (Table S3, ESI†). Despite their superior water-splitting performance, the oxygen electrocatalytic activity of these

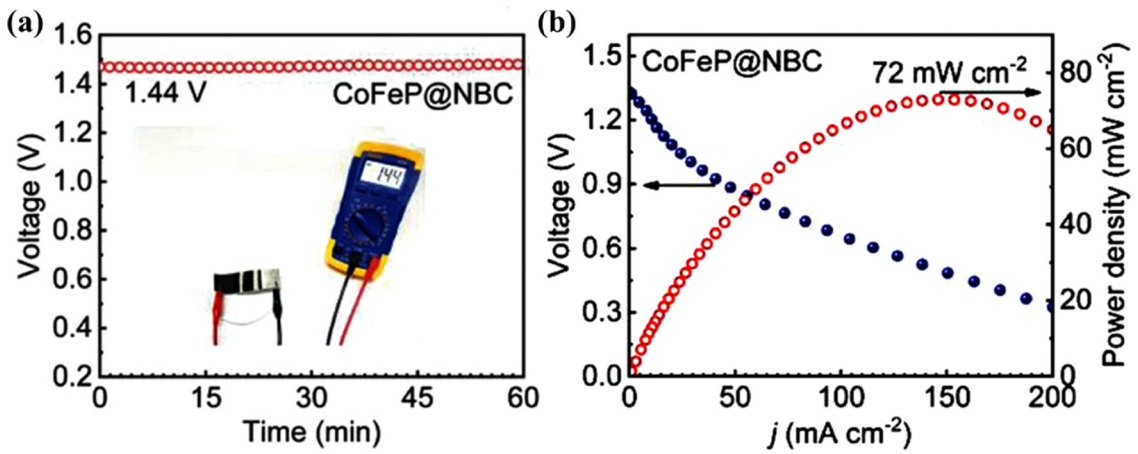

Fig. 12 (a) Plot illustrating the OCV of a quasi-solid-state ZAB based on CoFeP@NBC. (b) Discharge polarization and corresponding power densities curves of the quasi-solid-state ZAB. Inset in (a) is the digital image of the ZAB. Reproduced with permission from ref. 126. Copyright 2024 Wiley.

bimetallic TMPs remains relatively modest. The FeNiP bimetallic nanostructure supported on nitrogen- and phosphorus-doped carbon catalyzes the ORR and the OER at low overpotential.[132] OER current density as high as 100 mA cm^{-2} was achieved at an overpotential of 470 mV and a ΔE of 0.8 V, and is comparable to those of most of the monometallic phosphides. The specific capacity (602.7 mA h g^{-1}) and power density (163 mW cm^{-2}) obtained with the ZAB are not superior to those of the monometallic phosphide-based device. $FeCoP_2$ embedded into graphene-like carbon exhibited moderate bifunctionality with a ΔE of 0.814 V and battery performance with a maximum power density of 122.5 mW cm^{-2} and a charge–discharge cycle lifetime of 160 h.[128] In a recent study, MoCoP supported on nitrogen- and phosphorus-doped carbon showed outstanding electrocatalytic performance towards the ORR and OER with an ORR onset potential of 0.96 V and an OER current density of 50 mA cm^{-2} at an overpotential of 369 mV with an ΔE of 0.66 V.[129] The enhanced catalytic activity is attributed to increased surface hydrophilicity and electronic modulation resulting from the incorporation of molybdenum (Mo) as a second metal. Partial density of states (PDOS) analysis revealed (i) strong d–d orbital interactions between Co and Mo, which favor high electronic mobility, and (ii) an upward shift of the Co 3d orbitals toward the Fermi level, further enhancing catalytic performance. The MoCoP-based ZAB exhibited impressive cycling stability for 300 hours with an OCV of 1.50 V, outperforming ZABs based on monometallic phosphides (Fig. 13). The CoFeP bimetallic phosphide embedded in a N, P dual doped carbon matrix has been studied for both liquid and solid-state ZABs. The liquid ZAB exhibited a peak power density of 143.5 mW cm^{-2} and could run for more than 200 h during the charge–discharge cycle. The solid-state device displayed a peak power density of 72.6 mW cm^{-2}.[131]

The ORR activity of many bimetallic TMPs remains suboptimal, despite their notable performance in the OER. It is important to recognize that the mechanisms underlying the ORR and OER are fundamentally distinct, involving different active sites and complex multistep processes. Consequently, it is not reasonable to assume that all catalysts exhibiting strong OER activity will also demonstrate effective ORR activity. Design and synthesis of bimetallic TMPs with rationally selected metals that have distinct catalytic activity for the ORR and OER is required. Further investigations are also needed to elucidate the relationship between the electronic structure and the catalytic properties of these bimetallic phosphides.

5.2.3 Heterostructure engineering. The rational integration of an active catalyst with another catalyst is anticipated to enhance catalytic performance, likely due to synergistic effects arising from the interaction between the two components, the increased availability of active sites at the hetero-interface, and improved electrical conductivity. This synergistic effect is attributed to interfacial interactions that can either enhance existing catalytic properties or introduce entirely new catalytic functionalities. Heterostructured nanoelectrocatalysts

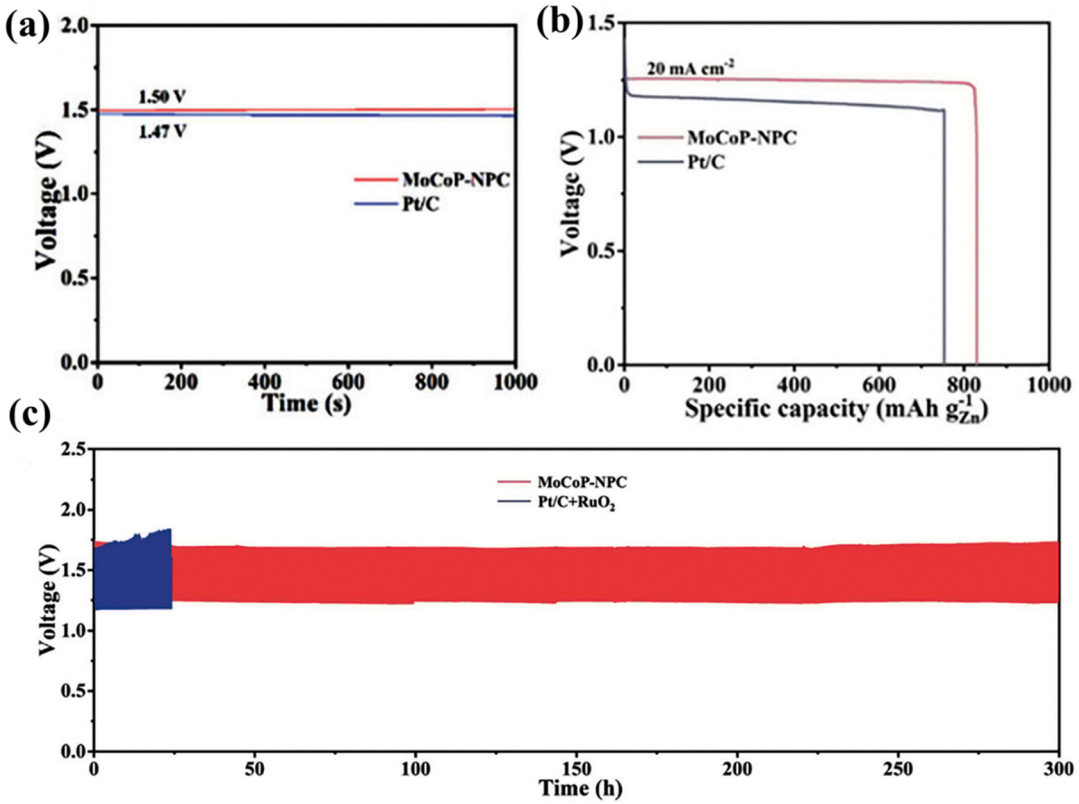

Fig. 13 Plots illustrating (a) the OCV, (b) discharge capacity, and (c) charge–discharge cycling stability of the MoCoP-NPC based rechargeable ZAB. Reproduced with permission from ref. 129. Copyright 2023 Wiley.

have been effectively utilized in electrochemical water splitting, with a notable example being a catalyst composed of Pt and $Ni(OH)_2$, which exhibited significantly improved HER activity compared to the state-of-the-art Pt catalyst.[133] Building on this concept, various other heterostructured electrocatalysts have been synthesized over the years for diverse catalytic and electrocatalytic applications.[134,135] Given the complex, multistep electron transfer processes involved in oxygen electrochemistry, the construction of multi-phase heterojunctions using TMPs combined with different active materials offers a synergistic effect that can effectively optimize the adsorption and desorption energies of reaction intermediates.[136] Heterostructured catalytic platforms comprising TMPs and nanostructured oxides, sulfides, nitrides, phosphides, and metals have demonstrated exceptional performance in water splitting and oxygen electrocatalysis.[105,137,138] Numerous TMPs have been heterostructured with another TMP, sulfides, nitrides, alloys, oxides, and doped carbon materials to achieve a wide range of tailored functional properties.[88,139–141]

The heterostructure based on V-doped crystalline Fe_2P and V-doped amorphous $FePO_x$ encapsulated in phosphorous-doped graphene (V-Fe_2P/$FePO_x$@PG) demonstrated to have enhanced catalytic performances towards the ORR ($E_{1/2}$ = 0.84 V) and OER (η_{10} = 270 mV).[142] The PDOS analysis showed a higher density of states at the Fermi energy level for the heterostructure compared to the individual counterpart (V-Fe_2P and V-$FePO_4$) supporting the enhanced electrical conductivity of V-Fe_2P/$FePO_4$. The bifunctional catalytic performance of the heterostructured catalyst was evaluated by fabricating an air cathode for ZABs. The energy device showed extended cycling stability for 600 h with a peak power density of 137 mW cm^{-2} and a specific capacity of 642 mA h g_{Zn}^{-1}. The synergistic effect between the crystalline V-Fe_2P core, amorphous $FePO_4$, and phosphorous-doped graphene accounts for enhanced catalytic activity and long-term durability. The ternary heterostructure consisting of FeP, Fe_2P, and Cu_3P coated with an ultrathin layer of phosphorus-doped carbon showed encouraging bifunctional activity with a ΔE of 0.74 V,[143] a high specific capacity of 815 mA h g_{Zn}^{-1} and a peak power density of 158 mW cm^{-2} with a long cycle life of 1100 cycles at 2 mA cm^{-2}. The carbon layer on the ternary heterostructure affords long cycling stability. The Co-based heterostructured phosphides are largely investigated for bifunctional oxygen electrocatalysis.[139,144–146] The interfacial interaction between CoP and Co_2P of the ZIF-derived CoP@Co_2P heterostructure supported on nitrogen and phosphorus-doped carbon network boosts the electron transfer kinetics of the oxygen electrocatalytic reactions.[145] The ZAB device based on this heterostructure delivered a high OCV of 1.56 V, a specific capacity of 689 mA h g^{-1}, and a peak power density of 215 mW cm^{-2} with outstanding charge–discharge cycling stability for >580 h. The interfacial interaction between the phosphides modulates the electronic structure and optimizes the adsorption of oxygen intermediates, facilitating the reaction kinetics. The modulation of the energy barrier for an efficient oxygen electrocatalytic reaction has recently been demonstrated by incorporating a Cu_3P/CoP heterostructure onto hollow porous nitrogen-doped carbon nanospheres.[146] The holistic structural optimization resulting from the favorable interactions between the two phosphides and the nitrogen-doped carbon yields a high turnover frequency of 2.62 s^{-1} at 0.85 V for the ORR. However, the ORR diffusion-limited current density is significantly below the theoretically expected 6 mA cm^{-2} at 1600 rpm. SCN poisoning tests indicate that the Cu_3P/CoP heterostructure is not well protected within the carbon shell, suggesting that the core heterostructure is primarily responsible for the observed catalytic activity. Theoretical studies reveal that strong coupling between the two phosphides reduces the energy barrier for the reaction. The ZAB device exhibits decent energy performance, showing a specific capacity of 765 mA h g_{Zn}^{-1} (~93% of the theoretical capacity of zinc) and cycling stability exceeding 300 hours. The chemical nature of heteroatoms doped onto the carbon support has a vital role in controlling the catalytic activity of the heterostructure.[147] The introduction of S onto the carbon network modulates the electronic properties of the N-doped carbon support and improves the electrocatalytic activity. The theoretical calculations showed that the carbon site connected to the S site is the main active site of the catalyst. The S-doping negatively shifts the d-band center of the carbon site making facile desorption of the adsorbed species, thereby enhancing the intrinsic activity of the catalyst. The integrated heterostructured catalyst with S- and N-doped carbon supports has good oxygen activity (ΔE = 0.684 V) and the ZAB has outstanding charge–discharge cycling stability for >900 h. The heterostructure engineering of CoP_3 with oxygen vacancy-rich CeO_2 regulates the electronic structure of CoP_3 and generates sufficient catalytically active sites for the OER/ORR.[148] The assembled ZAB delivered a large energy density (871 W h kg_{Zn}^{-1}) owing to the high specific surface area and improved electrical conductivity of the CoP_3/CeO_2/C catalyst. The role of CeO_2 is explained by the transformation that occurs between Ce^{3+} and Ce^{4+} states, which is responsible for reversible oxygen ion exchange and also acts as an effective buffer for the storage and release of oxygen.[149,150] The integration of metal nanoparticles with TMPs is a promising approach to improve the catalytic properties of TMPs due to charge transfer from the metal center to the heterojunction interface.[138,151,152] The heterostructured catalyst based on Co and Fe_2P embedded/encapsulated inside nitrogen and phosphorus-doped porous carbon has outstanding activity towards the ORR and OER with a ΔE of 0.685 V.[138] The catalyst is highly durable and retains >95% of the initial current for the ORR for a long period and the catalyst retains its phase purity after the durability test. The ZAB device delivered a maximum power density of 233 mW cm^{-2} and has superior charge–discharge cycling stability for >180 h. The coupling of Co with Fe_2P electronically optimizes the adsorption energy of the intermediate species due to possible charge transfer from Co to Fe_2P as illustrated by the theoretical studies (Fig. 14). The bamboo-like nitrogen-doped carbon nanotube confined-Co/Co_2P heterojunction catalyst obtained by the pyrolysis of ball-milled precursors containing cobalt salt, melamine, and TPP has profound catalytic activity.[153] The heterojunction catalyst highly favors the ORR with an $E_{1/2}$ = 0.9 V higher than that of the commercial Pt/C catalyst though the diffusion-limited current density is lower than the theoretical current density of 6 mA cm^{-2}. The self-reconstruction of the catalyst generates the OER active species

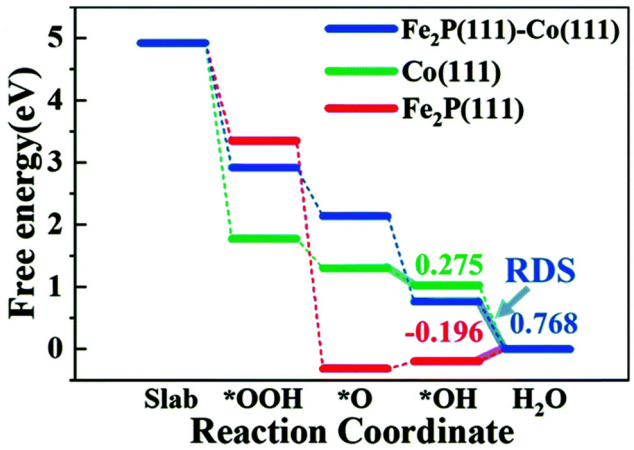

Fig. 14 The free energy diagram for $Fe_2P(111)$–Co(111), Co(111), and $Fe_2P(111)$. Reproduced with permission from ref. 138. Copyright 2022 Royal Society of Chemistry.

and efficiently catalyzes the OER. Interestingly the zinc–air flow battery showed outstanding charge–discharge cycling stability for >1000 h. The device maintained the charge–discharge voltage gap even after being shelved for 3 days, with no change in energy efficiency and delivered a maximum power density of 330 mW cm^{-2}. A major advantage of the zinc–air flow battery is its ability to significantly reduce dendritic growth, as the flowing electrolyte effectively rinses the anode surface and prevents the deposition of solid products and dendritic growth.

Recently, our group demonstrated the surface tailoring of nitrogen-doped carbon-encapsulated CoP (CoP@NC) nanostructures with an ultralow amount (0.56 atomic%) of Ru.[105] The surface-tailored heterostructure exhibited outstanding trifunctional electrocatalytic activity toward the ORR, OER, and HER (Fig. 15). The surface modification significantly shifted the ORR $E_{1/2}$ (66 mV positive shift) and increased the limiting current density by 26.8%. A notable decrease in ΔE (130 mV) supported the enhanced oxygen electrocatalytic performance induced by surface tailoring. The Ru particles modulated the electronic structure and boosted the catalytic activity. Strong synergistic electronic interactions through interfacial polarization between CoP and Ru nanoparticles promoted ORR and OER kinetics. The *in situ*-generated oxygen-containing species of high-valent Ru and Co served as active sites for the OER, while CoP, coupled with the encapsulating nitrogen-doped carbon, enhanced ORR activity. The experimental results aligned well with DFT calculations, which indicated that the introduction of Ru led to charge redistribution (Fig. 16) in the CoP nanostructure, thereby regulating the Gibbs free energy of the catalyst. Ru tailoring increased the density of states near the Fermi level, thereby improving electronic conductivity. The homemade ZAB device delivered a respectable specific capacity of 780 mA h g_{Zn}^{-1} and a high OCV of 1.51 V. The device retained its initial energy performance with a minimal voltage efficiency loss of 1.1% after 300 cycles. Interestingly, the heterostructured catalyst efficiently catalyzed the electrochemical water-splitting reaction, showing a low cell voltage of 1.47 V at 10 mA cm^{-2} and maintaining a stable current density of 25 mA cm^{-2} for 25 hours at 1.60 V.

6. Origin of bifunctional activity

The mechanism of oxygen electrocatalytic reactions involves multi-electrons and protons. Does TMPs directly participate in the electrocatalytic ORR and OER process? The literature on transition metal-based catalysts shows a major role of encapsulating or supporting heteroatom-doped carbon in promoting the electron transfer kinetics for the ORR though the contribution of the metal center cannot be denied. The ORR mechanistic studies with Co_2P/C supported on carbon black after subjecting the catalyst for 100 cycles of the ORR stability test showed the *in situ* formation of single-crystal Co_3O_4 with a (111) crystal face at the boundary of the Co_2P particles.[154] The O/Co ratio at the boundary was ≥1.33 corresponding to the ratio anticipated for Co_3O_4. The ratio of P/Co at the core of Co_2P remains 0.5 ascertaining that the inner core of the catalyst retained its chemical integrity. The ORR activity of Co_2P was attributed to the *in situ* generated Co_3O_4 overlayer. On the other hand, in our series of studies with heteroatom-doped

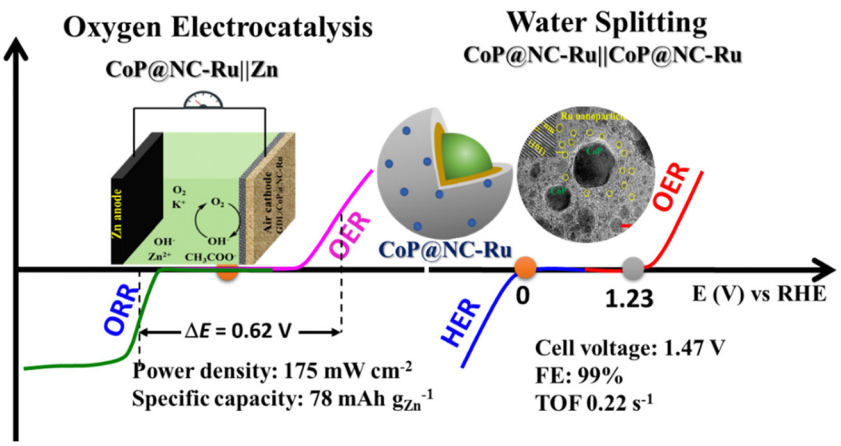

Fig. 15 Schematic illustration of bifunctional electrocatalytic performances of CoP@NC-Ru towards the ORR, OER, and HER. Adapted from ref. 105.

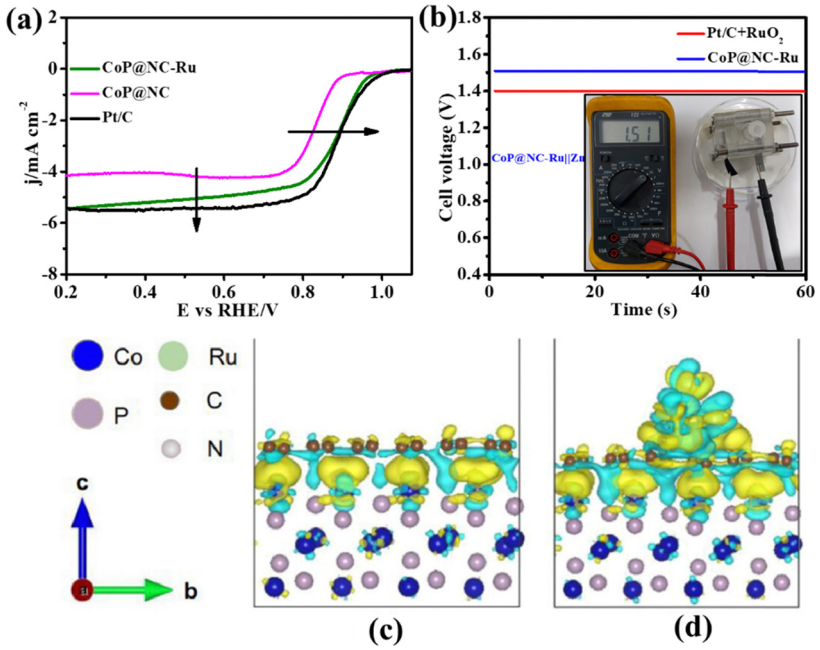

Fig. 16 (a) Electrocatalytic ORR activity of CoP@NC-Ru, (b) OCV of rechargeable ZABs. (c) and (d) Plot displaying the redistribution of charge density before (c) and after (d) surface trailing of CoP@NC with Ru. Reproduced with permission from ref. 105. Copyright 2024 American Chemical Society.

graphitic carbon encapsulated TMPs, the catalysts retained their chemical integrity even after extensive ORR durability tests.[62–64] It is well established by theoretical and experimental studies that the nature of nitrogen doped into the carbon network plays a crucial role in promoting the electron transfer kinetics of the ORR.[24–27,155] Besides N, S doped into the carbon network was also reported to contribute to the ORR activity. S modifies the electronic structure *via* interfacial interactions, thus, enhancing the catalytic activity of the C and N atoms, and optimizing the ORR dynamics.[147] The SCN^- poisoning test with a Cu_3P/CoP heterostructure showed the involvement of the metal center in the catalytic reaction.[146] The unprotected or exposed sites of the heterostructure are poisoned by the SCN^- anions. Consequently, a significant decrease in the limiting current and a negative shift of $E_{1/2}$ were observed due to the blocking of the active site by SCN^-, supporting the active participation of the metal center in the catalytic reaction. The SCN^- addition does not completely deactivate the catalyst, suggesting that the heteroatom-doped carbon shell does contribute to the ORR activity.[156] The metal coordinated with nitrogen synergistically catalyzes the ORR. Our earlier studies on the ORR with nitrogen-doped carbon-based materials supported the electrocatalytic effect of doped nitrogen.[155] Theoretical simulations predict a positive synergistic interaction between the N-doped carbon shell and the TMP core tunes the Gibbs free adsorption energies of the reaction intermediates.

The Pourbaix diagrams of transition metals and P show that TMPs have limited electrochemical stability in the high positive potential region. The transition metal and P species are not thermodynamically stable beyond OER onset potential (>1.23 V) at all the pHs. The corrosion of metals and the formation of a passive oxide or oxyhydroxide layer are inevitable. The formation of such a passive layer prevents the further dissolution of the metal. On the other hand, the P species transform into soluble species above the OER potential at all pHs. The leaching of P species and the *in situ* partial or complete transformation of metal species into oxide or oxyhydroxide species is now well established. The complete reconstruction of TMPs occurs only when the passivating layer is sufficiently thick. However, the TMPs undergo complete transformation when the potential is swept to a high positive side for an extended period of time.[157] These reactions can be kinetically slow depending on the nature of TMPs, electrolytes, and the extent of potential sweep. The TMPs serve as a pre-catalyst and the surface reconstruction of TMPs during positive potential sweep generates the corresponding metal oxide or oxyhydroxy species.[63] The *in situ* generated oxide or oxyhydroxide species serve as a catalyst for the OER. The XPS and XRD analyses of the post-OER durability test sample show a characteristic signature for metal-oxyhydroxide species and the loss of the XPS signature for P.[63] The unoxidized TMPs at the core often considered to afford good conductivity to the catalyst, enhancing the catalytic activity.

7. Summary and outlook

The operational principle of rechargeable ZABs involves the ORR and OER during discharge and charge. The bifunctional oxygen electrocatalytic reactions at the air cathode of ZABs largely decide the rechargeability of the energy device. A lower potential gap, ΔE, indicates that the air cathode is closer in efficiency to the oxygen electrode, with a smaller ΔE signifying excellent bifunctional activity. Achieving a small ΔE and long-

term charge–discharge cyclability while minimizing loss of voltaic efficiency is challenging. This feature article highlighted the use of TMPs as advanced bifunctional oxygen electrocatalysts for the development of rechargeable ZABs. We briefly discussed the fundamentals of ZABs, synthesis approaches for TMPs, their bifunctional activity, and ZAB performance. While pristine TMPs demonstrate limited catalytic efficiency for the ORR, they are recognized for their OER activity. However, the rationally engineered TMPs have shown promising bifunctional oxygen electrocatalytic performance. Among these, cobalt, nickel, and iron-based TMPs have been extensively studied.

Engineering TMPs through metal doping, creating anion/cation vacancies, and forming heterostructures with other materials (*e.g.*, sulfides, carbides, oxides, metals, and nitrides) modulates their electronic properties and enhances bifunctional catalytic activity. Encapsulating TMPs with heteroatom-doped graphitic carbon significantly improves durability and boosts the ORR activity through a synergistic effect. The charge transfer interactions between the heteroatoms and TMPs enhance catalytic performance and reduce ΔE, making these catalysts highly suitable for rechargeable ZABs. The carbon shell prevents loss of the electrochemically active surface area by suppressing unwanted catalyst aggregation and dissolution. Surface-tailoring of heteroatom-doped carbon-encapsulated TMPs with nanoscale metal particles optimizes the adsorption energy of oxygen intermediates, facilitating favorable adsorption and desorption.

A benchmarking protocol to evaluate the bifunctional activity of cathodes and the energy storage performance of ZABs is lacking in the literature. In evaluating the ORR activity of TMPs, the number of electrons transferred should be determined using rotating ring-disk electrode (RRDE) analysis rather than rotating disk electrode (RDE) analysis, as the number of electrons involved depends on the potential. Many studies inaccurately report electron transfer numbers based solely on RDE analysis, which is inappropriate for quantifying hydrogen peroxide production. Catalysts that promote the 4-electron reduction of oxygen to water are ideal for ZABs, as excessive hydrogen peroxide generation can impair overall performance. Furthermore, it is recommended (i) evaluating ORR and OER catalytic activity in terms of exchange current density rather than relying solely on the Tafel slope, as the latter is often misrepresented; (ii) calculating faradaic efficiency for the OER, as the oxidation of low-valent metals to high-valent states can contribute to current at high positive potentials; (iii) calibrating the RDE system, since the ORR limiting current density should not exceed the theoretical maximum of $\sim$6 mA cm^{-2} at 1600 rpm, contrary to some reported values ($>$6 mA cm^{-2}); and (iv) probing the surface structural changes of TMPs during the ORR and OER using in operando techniques. The kinetics of the ORR largely determines the discharge capacity of ZABs. Catalysts with sluggish ORR kinetics are suboptimal for ZAB applications. The role of heteroatom-doped carbon encapsulation in the OER remains poorly understood, and identifying active sites is crucial for elucidating the electron transfer mechanism in the ORR and its structure–property relationship. Therefore, establishing a comprehensive mechanism that links the structure and activity of various TMPs is essential. Advanced *in operando* studies could provide valuable mechanistic insights in this context. The stoichiometric ratio of metal to phosphorus (M/P) in TMPs significantly impacts their electrocatalytic performance. However, systematic exploration of the M/P ratio's effect on oxygen electrocatalysis is lacking, despite some studies demonstrating its influence in water splitting. Further investigations are needed to systematically examine the role of the M/P ratio in bifunctional oxygen electrocatalysis, enabling a deeper understanding of the correlation between the electronic structure and the catalytic properties.

Engineered TMPs exhibit remarkable catalytic and electron-transfer capabilities. However, they often fail to maintain structural integrity during prolonged operational cycles, particularly at high current densities. Surface oxidation of TMPs is a prevalent issue, leading to a decline in catalytic performance and, consequently, the charge storage efficiency over time. Suitable encapsulation of TMPs with a uniform thin layer of graphitic carbon can prevent such extensive surface oxidation. The choice of electrolyte significantly influences the charge storage performance of ZABs, including parameters such as energy density and lifespan. Currently, highly alkaline electrolytes (6 M KOH) are predominantly used in ZABs due to their ability to enhance catalytic activity. However, these electrolytes are corrosive to both the anode and cathode, which compromises long-term stability. In contrast, neutral or near-neutral electrolytes present an opportunity to mitigate corrosion and undesired side-product formation on the anode, potentially extending the ZAB lifespan. Nonetheless, the bifunctional oxygen electrocatalytic activity in neutral electrolytes is sluggish, highlighting the need for the development of suitable oxygen electrocatalysts that facilitate efficient electron transfer kinetics for both the ORR and OER. Additionally, the depth of discharge in rechargeable ZABs, an important parameter for practical applications, remains largely underexplored and warrants further investigation.[158,159] Currently, the lab-scale demonstration of ZABs for practical applications is limited to powering alkaline water splitting and desalination devices, digital timers, and charging supercapacitors.[27,31,63,160] Further works are essential to bring ZAB technology for industrial-scale applications.

Although numerous TMPs have been synthesized over the past decade, standardized protocols for their large-scale synthesis, crucial for the commercial development of ZAB technology, remain absent. Existing synthetic methods, such as hydrothermal and solid-state approaches, face several challenges, including high energy consumption, low yields, time-intensive processes, and uncontrolled growth of the product. Moreover, these methods present additional challenges, such as the need to remove capping agents in hydrothermal synthesis and the generation of toxic byproducts during solid-state synthesis. Consequently, the development of environmentally friendly, straightforward, and cost-effective methods for the large-scale synthesis of TMPs is urgently needed. Recent studies suggest that artificial intelligence (AI) and machine learning (ML) offer significant potential for the rational design and engineering of TMPs. These tools can facilitate the screening of catalytic activity and the evaluation of energy storage performance, thereby accelerating the commercialization of the ZAB technology.

Author contributions

S. G. coordinated the preparation and writing of the manuscript, conducted an extensive literature review, designed the table of contents (TOC), and proofread. R. C. contributed to the manuscript's writing, conducted the literature review, and assisted with proofreading. S. B. and M. M. K. contributed to proofreading. C. R. R. oversaw the manuscript's preparation and revision, contributed to writing and corrections, provided subject-matter expertise, and offered critical feedback to enhance the overall quality of the manuscript.

Data availability

The data supporting this feature review article can be found in the respective journals that have been cited in the manuscript and ESI.†

Conflicts of interest

There are no conflicts to declare.

Acknowledgements

The authors acknowledge financial support from the Science and Engineering Research Board (SERB) (CRG/2023/002307) and the Scheme for Transformational and Advanced Research in Science (STARS-2/2023-0186). Santanu Ghora thanks the Council of Scientific and Industrial Research, India, and IIT Kharagpur for the financial support. Dr Rishika Chakraborty acknowledges the receipt of the National Postdoctoral Fellowship (PDF/2023/000404).

References

1 United Nations, Department of Economic and Social Affairs, Population Division (2024). World Population Prospects 2024: Ten Key Messages. https://www.un.org/development/desa/pd/sites/www.un.org.development.desa.pd/files/key_messages_wpp_2024_20240709.pdf.
2 L. Yu, X. Zhou, L. Lu, X. Wu and F. Wang, *ChemSusChem*, 2020, **13**, 5361–5407.
3 Lithium-ion Battery Market Size, Share & Trends Analysis Report by Product (LCO, LFP, NCA, LMO, LTO, NMC), by Application (Consumer Electronics, Energy Storage Systems, Industrial), by Region, and Segment Forecasts, 2022-2030. Research and Markets. https://www.researchandmarkets.com/reports/4396452/lithium-ion-battery-market-size-share-and-trends.
4 B. Vedhanarayanan and K. C. Seetha Lakshmi, *Front. Battery Electrochem.*, 2024, **3**, 1377192.
5 P. Zhang, Y. Zhao and X. Zhang, *Chem. Soc. Rev.*, 2018, **47**, 2921–3004.
6 Y. Song, W. Li, K. Zhang, C. Han and A. Pan, *Adv. Energy Mater.*, 2024, **14**, 2303352.
7 S. Ren, X. Duan, S. Liang, M. Zhang and H. Zheng, *J. Mater. Chem. A*, 2020, **8**, 6144–6182.
8 Q. Wang, S. Kaushik, X. Xiao and Q. Xu, *Chem. Soc. Rev.*, 2023, **52**, 6139–6190.
9 X. W. Lv, Z. Wang, Z. Lai, Y. Liu, T. Ma, J. Geng and Z. Y. Yuan, *Small*, 2023, **20**, 2306396.
10 L. Maiché, *French Pat.*, 127069, 1878.
11 Z. Shao and X. Xu, *Zinc–Air Batteries: Introduction, Design Principles and Emerging Technologies*, John Wiley & Sons, Incorporated, Newark, 2023.
12 G. W. Heise and E. A. Schumacher, *Trans. Electrochem. Soc.*, 1932, **62**, 383–391.
13 R. Witherspoon, A Mechanically Rechargeable 1-KW Zinc-Air Battery, SAE Technical Paper 690204, 1969.
14 M. C. Cheiky, L. G. Danczyk and M. C. Wehrey, *Rechargeable Zinc–Air Batteries in Electric Vehicle Applications*, SAE International, 1990.
15 J. N. Liu, C.-X. Zhao, J. Wang, D. Ren, B. Q. Li and Q. Zhang, *Energy Environ. Sci.*, 2022, **15**, 4542–4553.
16 Batteries that breathe air, https://cen.acs.org/articles/95/i9/Batteries-breathe-air.html.
17 L. Collins, Recharge, New zinc-air battery is 'cheaper, safer and far longer-lasting than lithium-ion'. https://www.rechargenews.com/transition/new-zinc-air-battery-is-cheaper-safer-and-far-longer-lasting-than-lithium-ion/2-1-812068.
18 J. Qian, X. Liu, C. Zhong, G. Xu, H. Li, W. Zhou, B. You, F. Wang, D. Gao and D. Chao, *Adv. Funct. Mater.*, 2022, **33**, 2212021.
19 R. He, L. Yang, Y. Zhang, D. Jiang, S. Lee, S. Horta, Z. Liang, X. Lu, A. O. Moghaddam, J. Li, M. Ibanez, Y. Xu, Y. Zhou and A. Cabot, *Adv. Mater.*, 2023, **35**, 2303719.
20 J. Zhang, Q. Zhou, Y. Tang, L. Zhang and Y. Li, *Chem. Sci.*, 2019, **10**, 8924–8929.
21 T. Zhou, N. Zhang, C. Wu and Y. Xie, *Energy Environ. Sci.*, 2020, **13**, 1132–1153.
22 A. M. Yao and V. Viswanathan, *J. Phys. Chem. Lett.*, 2024, **15**, 1143–1151.
23 M. Liu, X. Lv, Z. Mi, S. Chen, J. Li, J. Wu, T. Sun, L. Zhang and J. Zhang, *ACS Appl. Energy Mater.*, 2023, **6**, 7317–7322.
24 A. Samanta, A. Ghatak, S. Bhattacharyya and C. R. Raj, *Electrochim. Acta*, 2020, **348**, 136274.
25 A. Samanta and C. R. Raj, *J. Power Sources*, 2020, **455**, 227975.
26 A. Samanta and C. R. Raj, *J. Phys. Chem. C*, 2018, **122**, 15843–15852.
27 A. Kundu, A. Samanta and C. R. Raj, *ACS Appl. Mater. Interfaces*, 2021, **13**, 30486–30496.
28 D. Ji, L. Fan, L. Tao, Y. Sun, M. Li, G. Yang, T. Q. Tran, S. Ramakrishna and S. Guo, *Angew. Chem., Int. Ed.*, 2019, **58**, 13840–13844.
29 B. Liu, Y. Wang, H. Peng, R. Yang, Z. Jiang, X. Zhou, C. Lee, H. Zhao and W. Zhang, *Adv. Mater.*, 2018, **30**, 1803144.
30 Q. Lu, X. H. Zou, C. Wang, K. M. Liao, P. Tan, R. Ran, W. Zhou, M. Ni and Z. P. Shao, *Energy Storage Mater.*, 2021, **39**, 11–20.
31 S. Mallick, A. Samanta and C. R. Raj, *Sustainable Energy Fuels*, 2020, **4**, 4008–4017.
32 X. F. Lu, S. L. Zhang, E. Shangguan, P. Zhang, S. Gao and X. W. Lou, *Adv. Sci.*, 2020, **7**, 2001178.
33 A. Baby, D. Singh, C. Murugesan and P. Barpanda, *Chem. Commun.*, 2020, **56**, 8400–8403.
34 S. Carenco, D. Portehault, C. Boissiere, N. Mezailles and C. Sanchez, *Chem. Rev.*, 2013, **113**, 7981–8065.
35 R. Chakraborty and M. Pradhan, Phosphides and nitrides for visible light photocatalysis, *Nanostructured Materials for Visible Light Photocatalysis*. Elsevier, 2022, pp. 197–250.
36 N. Khodayar, A. Noori, M. S. Rahmanifar, M. Moloudi, N. Hassani, M. N. Amal, M. F. E. Kady, N. B. Mohamed, X. Xia, Y. Zhang, R. B. Kaner and M. F. Mousavi, *Energy Environ. Sci.*, 2024, **17**, 5200–5215.
37 B. Owens-Baird, Y. V. Kolenko and K. Kovnir, *Chem. – Eur. J.*, 2018, **24**, 7298–7311.
38 S. T. Oyama, T. Gott, H. Zhao and Y. K. Lee, *Catal. Today*, 2009, **143**, 94–107.
39 L. K. Putri, B. J. Ng, R. Y. Z. Yeo, W. J. Ong, A. R. Mohamed and S. P. Chai, *Chem. Eng. J.*, 2023, **461**, 141845.
40 X. Liu, J. Huang, T. Li, W. Chen, G. Chen, L. Han and K. Ostrikov, *J. Mater. Chem. A*, 2022, **10**, 13448–13455.
41 B. R. Wygant, K. Kawashima and C. B. Mullins, *ACS Energy Lett.*, 2018, **3**, 2956–2966.
42 J. Kupka and A. Budniok, *J. Appl. Electrochem.*, 1990, **20**, 1015–1020.
43 A. E. Henkes, Y. Vasquez and R. E. Schaak, *J. Am. Chem. Soc.*, 2007, **129**, 1896–1897.
44 S. C. Perera, P. S. Fodor, G. M. Tsoi, L. E. Wenger and S. L. Brock, *Chem. Mater.*, 2003, **15**, 4034–4038.
45 S. C. Perera, G. Tsoi, L. E. Wenger and S. L. Brock, *J. Am. Chem. Soc.*, 2003, **125**, 13960–13961.
46 J. Park, B. Koo, K. Y. Yoon, Y. Hwang, M. Kang, J.-G. Park and T. Hyeon, *J. Am. Chem. Soc.*, 2005, **127**, 8433–8440.
47 J. Park, B. Koo, Y. Hwang, C. Bae, K. An, J. G. Park, H. M. Park and T. Hyeon, *Angew. Chem., Int. Ed.*, 2004, **116**, 2332–2335.
48 Z. Wang, S. Liu, J. Du, Y. Xing, Y. Hu, Y. Ma, X. Lu and C. Wang, *Green Chem.*, 2024, **26**, 7779–7788.

49 T. Su'a, M. N. Poli and S. L. Brock, *ACS Nanosci. Au*, 2022, **2**, 503–519.
50 S. Ghosh, S. R. Kadam, L. Houben, R. Bar-Ziv and M. Bar-Sadan, *Appl. Mater. Today*, 2020, **20**, 100693.
51 D. H. Ha, L. M. Moreau, C. R. Bealing, H. Zhang, R. G. Hennig and R. D. Robinson, *J. Mater. Chem.*, 2011, **21**, 11498–11510.
52 N. P. Sweeny, C. S. Rohrer and O. W. Brown, *J. Am. Chem. Soc.*, 1958, **80**, 799–800.
53 B. F. Stein and R. H. Walmsley, *Phys. Rev.*, 1966, **148**, 933–939.
54 J. Schieferecke and D. Worley, *J. Anal. Appl. Pyrolysis*, 2004, **71**, 47–50.
55 S. Yang, K. Zhang, A. G. Ricciardulli, P. Zhang, Z. Liao, M. R. Lohe, E. Zschech, P. W. Blom, W. Pisula, K. Müllen and X. Feng, *Angew. Chem., Int. Ed.*, 2018, **130**, 4767–4771.
56 Z. Liu, S. Yang, B. Sun, P. Yang, J. Zheng and X. Li, *Angew. Chem., Int. Ed.*, 2020, **132**, 1991–1995.
57 R. H. Bowker, M. C. Smith, M. L. Pease, K. M. Slenkamp, L. Kovarik and M. E. Bussell, *ACS Catal.*, 2011, **1**, 917–922.
58 Q. Guan, W. Li, M. Zhang and K. Tao, *J. Catal.*, 2009, **263**, 1–3.
59 X. Wang, P. Clark and S. T. Oyama, *J. Catal.*, 2002, **208**, 321–331.
60 M. H. Lee, D. H. Youn and J. S. Lee, *Appl. Catal., A*, 2020, **594**, 117451.
61 S. Chakrabartty, D. Sahu and C. R. Raj, *ACS Appl. Energy Mater.*, 2020, **3**, 2811–2820.
62 M. M. Kumar and C. R. Raj, *ACS Appl. Nano Mater.*, 2019, **2**, 643–648.
63 M. M. Kumar and C. R. Raj, *ACS Appl. Mater. Interfaces*, 2022, **14**, 15176–15186.
64 M. M. Kumar, R. Singh and C. R. Raj, *Chem. – Eur. J.*, 2024, e202400684, DOI: **10.1002/asia.202400684**.
65 S. Chakrabartty, B. K. Barman and C. R. Raj, *Chem. Commun.*, 2019, **55**, 4399–4402.
66 T. C. Ehlert and M. M. Hsia, *J. Chem. Eng. Data*, 1972, **17**, 18–21.
67 T. Wu, M.-Y. Han and Z. J. Xu, *ACS Nano*, 2022, **16**, 8531–8539.
68 I. A. Liyanage, A. V. Flores and E. G. Gillan, *Inorg. Chem.*, 2023, **62**, 4947–4959.
69 P. E. R. Blanchard, A. P. Grosvenor, R. G. Cavell and A. Mar, *Chem. Mater.*, 2008, **20**, 7081–7088.
70 N. Coleman, Jr., M. D. Lovander, J. Leddy and E. G. Gillan, *Inorg. Chem.*, 2019, **58**, 5013–5024.
71 Z. Guo, R. Wang, Y. Guo, J. Jiang, Z. Wang, W. Li and M. Zhang, *ACS Catal.*, 2022, **12**, 15193–15206.
72 Y. Liu, C. Li, M. Yuan, X. H. Zhang, H. K. Lan, Y. T. Chen, M. G. Tian, K. Liu and L. Wang, *Catal. Sci. Technol.*, 2023, **13**, 3084–3093.
73 J. Yang, D. Guo, S. Zhao, Y. Lin, R. Yang, D. Xu, N. Shi, X. Zhang, L. Lu, Y.-Q. Lan, J. Bao and M. Han, *Small*, 2019, **15**, 1804546.
74 A. Brenner, D. E. Couch and E. K. Williams, *J. Res. Natl. Bur. Stand.*, 1950, **44**, 109–122.
75 E. Tóth-Kádár, I. Bakonyi, A. Sólyom, J. Hering, G. Konczos and F. Pavlyák, *Surf. Coat. Technol.*, 1987, **31**, 31–43.
76 I. Paseka, *Electrochim. Acta*, 1995, **40**, 1633–1640.
77 A. Budniok and P. Matyja, *Thin Solid Films*, 1991, **201**, 305–315.
78 A. B. Silva, M. Medina, L. A. Goulart and L. H. Mascaro, *Electrochim. Acta*, 2024, **475**, 143679.
79 A. Meng, H. Zhang, B. Huangfu, W. Tian, L. Sheng, Z. Li, S. Tan and Q. Li, *Prog. Nat. Sci.: Mater. Int.*, 2020, **30**, 461–468.
80 K. D. Bharathi and A. K. Mohanakrishnan, *Chem. Commun.*, 2024, **60**, 3838.
81 M. Asnavandi, B. H. R. Suryanto, W. Yang, X. Bo and C. Zhao, *ACS Sustainable Chem. Eng.*, 2018, **6**, 2866–2871.
82 Y. S. Park, W. S. Choi, M. J. Jang, J. H. Lee, S. Park, H. Jin, M. H. Seo, K. H. Lee, Y. Yin, Y. Kim, J. Yang and S. M. Choi, *ACS Sustainable Chem. Eng.*, 2019, **7**, 10734–10741.
83 G. B. Darband, M. Aliofkhazraei, S. Hyun and S. Shanmugam, *ACS Appl. Mater. Interfaces*, 2020, **12**, 53719–53730.
84 A. Brenner, *Electrodeposition of Alloys*, Academic Press, New York, 1963, vol. 1 and 2.
85 J. L. Carbajal and R. E. White, *J. Electrochem. Soc.*, 1988, **135**, 2952–2957.
86 A. Lelevic and F. C. Walsh, *Surf. Coat. Technol.*, 2019, **369**, 198–220.
87 G. B. Darband, *Curr. Opin. Electrochem.*, 2024, **46**, 101507.
88 C. C. Yao, J. X. Li, Z. H. Zhang, C. L. Gou, Z. S. Zhang, G. Pan and J. Zhang, *Small*, 2022, **18**, 2108094.
89 N. Thakur, M. Kumar, D. Mandal and T. C. Nagaiah, *ACS Appl. Mater. Interfaces*, 2021, **13**, 52487–52497.
90 L. Cheng, Z. Zhang, W. Niu, G. Xu and L. Zhu, *J. Power Sources*, 2008, **182**, 91–94.
91 Z. Liu, N. Li, H. Zhao, Y. Zhang, Y. Huang, Z. Yin and Y. Du, *Chem. Sci.*, 2017, **8**, 3211–3217.
92 Y. Ma, H. Li, H. Wang, S. Ji, V. Linkov and R. Wang, *J. Power Sources*, 2014, **259**, 87–91.
93 M. Ledendecker, S. Krick Calderón, C. Papp, H. P. Steinrück, M. Antonietti and M. Shalom, *Angew. Chem., Int. Ed.*, 2015, **54**, 12361–12365.
94 K. Chen, X. Huang, C. Wan and H. Liu, *RSC Adv.*, 2015, **5**, 92893–92898.
95 C. Han, X. Bo, Y. Zhang, M. Li, A. Wang and L. Guo, *Chem. Commun.*, 2015, **51**, 15015–15018.
96 N. Jiang, B. You, M. Sheng and Y. Sun, *Angew. Chem., Int. Ed.*, 2015, **54**, 6251–6254.
97 V. V. T. D. Nguyen, S. Zhang, E. B. Trigg, R. Agarwal, J. Li, D. Su, K. I. Winey and C. B. Murray, *ACS Nano*, 2015, **9**, 8108–8115.
98 X. Zhong, Y. Jiang, X. Chen, L. Wang, G. Zhuang, X. Li and J. G. Wang, *J. Mater. Chem. A*, 2016, **4**, 10575–10584.
99 S. H. Ahn and A. Manthiram, *Small*, 2017, **13**, 1702068.
100 J. Gao, J. Wang, L. Zhou, X. Cai, D. Zhan, M. Hou and L. Lai, *ACS Appl. Mater. Interfaces*, 2019, **11**, 10364–10372.
101 J. Hu, Y. Qin, H. Sun, Y. Ma, L. Lin, Y. Peng, J. Zhong, M. Chen, X. Zhao and Z. Deng, *Small*, 2022, **18**, 2106260.
102 P. X. Zhang, Y. Y. Liu, S. L. Wang, L. M. Zhou, T. Liu, K. Sun, H. Q. Cao, J. C. Jiang, X. L. Wu and B. J. Li, *Small*, 2022, **18**, 2202725.
103 X. Wu, T. Zhou, G. Han, S. Liu, M. Cao, S. Li, J. Wang, Y. Liu, J. Jiang, Y. Wang and B. Li, *Sustainable Energy Fuels*, 2024, **8**, 1983–1991.
104 R. Z. Zhang, C. M. Zhang and W. Chen, *J. Mater. Chem. A*, 2016, **4**, 18723–18729.
105 M. M. Kumar, C. Aparna, A. K. Nayak, U. V. Waghmare, D. Pradhan and C. R. Raj, *ACS Appl. Mater. Interfaces*, 2024, **16**, 3542–3551.
106 M. Li, L. Chen, S. Ye, G. Fan, L. Yang, X. Zhang and F. Li, *J. Mater. Chem. A*, 2019, **7**, 13695–13704.
107 H. Liang, M. Xu and E. Asselin, *J. Power Sources*, 2021, **510**, 230387.
108 J. Lv, S. C. Abbas, Y. Huang, Q. Liu, M. Wu, Y. Wang and L. Dai, *Nano Energy*, 2018, **43**, 130–137.
109 X. Guo, C. Lv, Y. Wang, T. Wang, X. Gan, L. Li and X. Lv, *Chem. – Eur. J.*, 2023, **29**, e202302182.
110 Y. X. Wang, J. X. Liu, T. Lu, R. He, N. N. Xu and J. L. Qiao, *Appl. Catal., B*, 2023, **321**, 122041.
111 Z.-Z. Liu, N. Yu, R.-Y. Fan, B. Dong and Z. F. Yan, *Nanoscale*, 2024, **16**, 1080–1101.
112 X. Wang, X. Liu, S. Wu, K. Liu, X. Meng, B. Li, J. Lai, L. Wang and S. Feng, *Nano Energy*, 2023, **109**, 108292.
113 Y. Dong, X. Chen, B. Yu, W. Zhang, X. Zhu and Z. Liu, *J. Alloys Compd.*, 2022, **905**, 164023.
114 J. W. Zhu, J. Q. Chi, T. Cui, L. L. Guo, S. Q. Wu, B. Li, J. P. Lai and L. Wang, *Appl. Catal., B*, 2023, **328**, 122487.
115 S. Li, Z. Geng, X. Wang, X. Ren, J. Liu, X. Hou, Y. Sun, W. Zhang, K. Huang and S. Feng, *Chem. Commun.*, 2020, **56**, 2602–2605.
116 J. Qi, T. Xu, J. Cao, S. Guo, Z. Zhong and J. Feng, *Nanoscale*, 2020, **12**, 6204–6210.
117 W. L. Kwong, E. G. Espino, C. C. Lee, R. Sandström, T. Wågberg and J. Messinger, *ChemSusChem*, 2017, **10**, 4544–4551.
118 J. H. Shi, F. Qiu, W. B. Yuan, M. M. Guo and Z. H. Lu, *Chem. Eng. J.*, 2021, **403**, 126312.
119 Y. Feng, R. Wang, P. Dong, X. Wang, W. Feng, J. Chen, L. Cao, L. Feng, C. He and J. Huang, *ACS Appl. Mater. Interfaces*, 2021, **13**, 48949–48961.
120 Z. Z. Liu, N. Y. R. Y. Fan, B. Dong and Z. F. Yan, *Nanoscale*, 2024, **16**, 1080–1101.
121 J. Tong, H. Wang, L. Bo, C. Li, X. Guan, D. Kong, Y. Zhang, W. Shi and Z. Lei, *Mater. Res. Bull.*, 2022, **147**, 111638.
122 X. W. Gao, J. J. Mu, R. Wei, X. Wang, Q. Gu, L. K. Zhao and W. B. Luo, *Small Methods*, 2024, **8**, 2301645.
123 X. Hu, G. Luo, X. Guo, Q. Zhao, R. Wang, G. Huang, B. Jiang, C. Xu and F. Pan, *Sci. Bull.*, 2021, **66**, 708–719.
124 M. Ding, X. Hui and L. Yin, *Electrochim. Acta*, 2023, **468**, 142891.
125 L. Diao, T. Yang, B. Chen, B. Zhang, N. Zhao, C. Shi, E. Liu, L. Ma and C. He, *J. Mater. Chem. A*, 2019, **7**, 21232–21243.

126 P. Zhang, S. Liu, J. Zhou, L. Zhou, B. Li, S. Li, X. Wu, Y. Chen, X. Li, X. Sheng, Y. Liu and J. Jiang, *Small*, 2024, **20**, 2307662.
127 L. Zhang, S. H. Luo, P. Li, L. Qian, P. Li and S. Yan, *Int. J. Hydrogen Energy*, 2024, **53**, 49–59.
128 R. Liu, Y. Wang, W. Zheng, H. Zhang and Z. Zhang, *Energy Fuels*, 2023, **37**, 1344–1352.
129 S. Zhao, S. Ran, N. Shi, M. Liu, W. Sun, Y. Yu and Z. Zhu, *Small*, 2023, **19**, 2302414.
130 W. Chen, S. Chang, H. Yu, W. Li, H. Zhang and Z. Zhang, *Nanoscale*, 2021, **13**, 17136–17146.
131 L. Gao, S. Chang and Z. Zhang, *ACS Appl. Mater. Interfaces*, 2021, **13**, 22282–22291.
132 J. T. Ren, Y. S. Wang, L. Chen, L. J. Gao, W. W. Tian and Z. Y. Yuan, *Chem. Eng. J.*, 2020, **389**, 124408.
133 R. Subbaraman, D. Tripkovic, D. Strmcnik, K. C. Chang, M. Uchimura, A. P. Paulikas, V. Stamenkovic and N. M. Markovic, *Science*, 2011, **334**, 1256–1260.
134 H. Wang, W. Fu, X. Yang, Z. Huang, J. Li, H. Zhang and Y. Wang, *J. Mater. Chem. A*, 2020, **8**, 6926–6956.
135 W. Wu, S. Luo, Y. Huang, H. He, P. K. Shen and J. Zhu, *Mater. Chem. Front.*, 2024, **8**, 1064–1083.
136 X. Luo, P. Ji, P. Wang, R. Cheng, D. Chen, C. Lin, J. Zhang, J. He, Z. Shi, N. Li, S. Xiao and S. Mu, *Adv. Energy Mater.*, 2020, **10**, 1903891.
137 H. Zhang, A. W. Maijenburg, X. Li, S. L. Schweizer and R. B. Wehrspohn, *Adv. Funct. Mater.*, 2020, **30**, 2003261.
138 Y. Bai, Y. Wang, Z. Qiao, Y. Yang, L. Deng, C. Li, X. Chen, S. Wang, Y. Huang, X. Zhang and D. Cao, *J. Mater. Chem. A*, 2022, **10**, 16037–16045.
139 K. Chen, L. Wang, J. Long, F. Zhao and L. Kang, *Chem. Eng. J.*, 2024, **496**, 153820.
140 W. Sun, Y. Xu, P. Yin and Z. Yang, *Appl. Surf. Sci.*, 2021, **554**, 149670.
141 Q. Shi, Y. Zheng, W. Li, B. Tang, L. Qin, W. Yang and Q. Liu, *Catal. Sci. Technol.*, 2020, **10**, 5060–5068.
142 Q. P. Ngo, T. T. Nguyen, M. Singh, R. Balaji, N. H. Kim and J. H. Lee, *Appl. Catal., B*, 2023, **331**, 122674.
143 X. Yang, F. Wang, Z. Jing, M. Chen, B. Wang, L. Wang, G. Qu, Y. Kong and L. Xu, *Small*, 2023, **19**, 2301985.
144 X. Lv, W. Tian, Y. Liu and Z. Y. Yuan, *Mater. Chem. Front.*, 2019, **3**, 2428.
145 Z. Li, Y. Zeng, D. Xiong, L. Zhou, J. Zhou, Y. Yang, F. Zhan, K. Wang, Y. Du and Y. Liu, *Inorg. Chem. Front.*, 2024, **11**, 549–561.
146 M. Guo, L. Wang, Z. Huang, H. Li, T. T. Isimjan and X. Yang, *ACS Nano*, 2024, **18**, 17901–17912.
147 Y. Liu, J. Y. Gao, M. Yuan, H. D. Li, Y. T. Chen, Y. M. Du, Z. Y. Xiao, K. Liu and L. Wang, *Inorg. Chem.*, 2024, **63**, 7926–7936.
148 J. Li, Y. Kang, Z. Lei and P. Liu, *Appl. Catal., B*, 2023, **321**, 122029.
149 Y. Liu, C. Ma, Q. Zhang, W. Wang, P. Pan, L. Gu, D. Xu, J. Bao and Z. Dai, *Adv. Mater.*, 2019, **31**, 1900062.
150 J. Chen, N. Zhou, H. Wang, Z. Peng, H. Li, Y. Tang and K. Liu, *Chem. Commun.*, 2015, **51**, 10123–10126.
151 X. Liu, J. Wu, Z. Luo, P. Liu, Y. Tian, X. Wang and H. Li, *ACS Appl. Mater. Interfaces*, 2023, **15**, 9240–9249.
152 Q. P. Ngo, T. T. Nguyen, M. Singh, N. H. Kim and J. H. Lee, *J. Mater. Chem. A*, 2024, **12**, 1185–1199.
153 M. Wu, G. Zhang, N. Chen, Y. Hu, T. Regier, D. Rawach and S. Sun, *ACS Energy Lett.*, 2021, **6**, 1153–1161.
154 A. P. Puerto, K. L. Ng, K. Fahy, A. E. Goode, M. P. Ryan and A. Kucernak, *ACS Catal.*, 2019, **9**, 11515–11529.
155 S. Bag and C. R. Raj, *J. Chem. Sci.*, 2016, **128**, 339–347.
156 Y. Yu, J. Ma, C. Chen, Y. Fu, Y. Wang, K. Li, Y. Liao, L. Zheng and X. Zuo, *ChemCatChem*, 2019, **11**, 1722–1731.
157 W. Li, D. Xiong, X. Gao and L. Liu, *Chem. Commun.*, 2019, **55**, 8744–8763.
158 B. J. Hopkins, C. N. Chervin, J. W. Long, D. R. Rolison and J. F. Parker, *ACS Energy Lett.*, 2020, **5**, 3405–3408.
159 D. Deckenbach and J. J. Schneider, *Adv. Mater. Interfaces*, 2023, **10**, 2202494.
160 J. Gao, D. Pan, K. Chen, Y. Liu, J. Chen and Z. Wen, *Adv. Energy Mater.*, 2024, **14**, 2400368.